Cerebral cortical circuitry formation requires functional glycine receptors

Giovanni Morelli[1,2,3], Ariel Avila[5], Stylianos Ravanidis[1], Najat Aourz[6], Rachael L. Neve[7], Ilse Smolders[6], Robert J. Harvey[8], Jean-Michel Rigo[1*], Laurent Nguyen[2,3,4*], Bert Brône[1*]

[1]BIOMED Research Institute, Hasselt University, Hasselt 3500, Belgium; [2]GIGA-Neurosciences; [3]Interdisciplinary Cluster for Applied Genoproteomics (GIGA-R), [4]Walloon Excellence in Lifesciences and Biotechnology (WELBIO), University of Liège, C.H.U. Sart Tilman, Liège 4000, Belgium; [5]Program in Neurosciences and Mental Health, SickKids Research Institute, The Hospital for Sick Children (SickKids), Toronto, ON M5G 1X8, Canada; [6]Department of Pharmaceutical Chemistry and Drug Analysis, C4N, Center for Neuroscience, Vrije Universiteit Brussel, Laarbeeklaan 103, 1090 Brussel, Belgium; [7]Department of Brain and Cognitive Sciences, Massachusetts Institute of Technology, Cambridge, MA 02139; [8]Department of Pharmacology, UCL School of Pharmacy, 29-39 Brunswick Square, London WC1N 1AX, United Kingdom.

* *These senior authors contributed equally to the work*

Corresponding authors: bert.brone@uhasselt.be, jeanmichel.rigo@uhasselt.be, lnguyen@ulg.ac.be

Running title: GlyRα2 controls cortical circuitry development

Abstract

The development of the cerebral cortex is a complex process that requires the generation, migration, and differentiation of neurons. Interfering with any of these steps can impair the establishment of connectivity and, hence, function of the adult brain. Neurotransmitter receptors have emerged as critical players to regulate these biological steps during brain maturation. Among them, α2 subunit-containing glycine receptors (GlyRs) regulate cortical neurogenesis and the present work demonstrates the long-term consequences of their genetic disruption on neuronal connectivity in the postnatal cerebral cortex. Our data indicate that somatosensory cortical neurons of Glra2 knockout mice (Glra2KO) have more dendritic branches with an overall increase in total spine number. These morphological defects correlate with a disruption of the excitation/inhibition balance, thereby increasing network excitability and enhancing susceptibility to epileptic seizures after pentylenetetrazol tail infusion. Taken together, our findings show that the loss of embryonic GlyRα2 ultimately impairs the formation of cortical circuits in the mature brain.

Introduction

The cerebral cortex is an evolutionary advanced structure of the brain that processes sensory information, controls motor output and mediates higher-order cognitive functions. Its well-orchestrated development extends from embryogenesis to postnatal stages (Lui et al., 2011) and involves a tight regulation of birth, migration and differentiation of several subtypes of neurons into six layers (Rakic et al., 1994, Rakic, 2009, Lui et al., 2011). Disruption of this cellular regulatory logic is often associated with the etiology of epilepsy, autism spectrum disorder (ASD), schizophrenia, and intellectual disabilities (Lee et al., 1997, Lewis and Levitt, 2002, Valiente and Marin, 2010, Geschwind and Rakic, 2013, Pilorge et al., 2015). A prominent trait of the cerebral cortex is its complex cellular architecture, which relies on its high degree of neuronal diversity (Greig et al., 2013). Cortical neurons are generated during development and can be canonically subdivided into projection neurons (PNs), which forward excitatory signals and the interneurons (INs), which relay inhibition in the cortical circuitry (Molyneaux et al., 2007, Huang, 2014). Growth of cortical neuron dendritic arborization accelerates during the early postnatal developmental window leading to a thickening of the developing cortex, which further coincides with an increase rate of synaptogenesis (Huttenlocher, 1979, Huttenlocher and Dabholkar, 1997). Indeed, cortical neurons initially established high numbers of synapses that are progressively eliminated during development to form stable mature circuitry in the adult cerebral cortex (Huttenlocher, 1979, Huttenlocher and Dabholkar, 1997, Harris and Mrsic-Flogel, 2013).

Several lines of evidence indicate that the microenvironment of the developing cortex plays instructive roles during embryogenesis. Along this line, neurotransmitters have a central role during corticogenesis (Ruediger and Bolz, 2007) and disrupting their signaling accounts for impaired brain functions resulting from either reduction, misplacement or poor maturation of specific neuronal populations in the cortex (Represa and Ben-Ari, 2005, Avila et al., 2013a,

Avila et al., 2013b, Avila et al., 2014). GlyRs are ligand-gated chloride channels expressed in the cerebral cortex either as homopentamers of α subunits, or as complexes of two α and three β subunits (Betz and Laube, 2006). Four α subunit isoforms (α1-α4) and one β subunit variant have been identified and significant progress has been made in the understanding of the biological roles of GlyRs via studies of mutant mice (Malosio et al., 1991, Flint et al., 1998, Betz and Laube, 2006, Avila et al., 2013b, Avila et al., 2014). Most cortical GlyRs are α2 homomers during embryogenesis and at birth (Young-Pearse et al., 2006). Moreover, recent work reported the integration of α3 subunits in GlyRs expressed by neurons from layers II/III and also V and VI of the somatosensory cortex (Sorensen et al., 2013). However, physiological studies of GlyRs in PNs of layer II/III and V/VI of the prefrontal cortex indicated a lack of glycinergic synapses, rather suggesting that GlyRs were tonically activated in PNs (Liu et al., 2014, Salling and Harrison, 2014). Interestingly, α2 subunit GlyRs are pivotal for brain development. Both cortical PNs and INs express functional GlyRs during embryogenesis (Flint et al., 1998, Avila et al., 2013b, Avila et al., 2014) and genetic inactivation of *Glra2* disrupted dorsal cortical progenitor homeostasis. This defect resulted in a global reduction of PNs number that settle in the upper or deep layers of the cerebral cortex. Overall, the depletion of cortical neurons observed in *Glra2*KO embryos contributes to moderate microcephaly in newborn mice (Avila et al., 2014). Furthermore, disruption of GlyR activity impairs tangential migration of INs from the medial ganglionic eminence (MGE) to the cerebral cortex, thus leading to an overall reduction of INs at birth (Avila et al., 2013b, Avila et al., 2014). Loss of function mutations of *Glra2* are associated with ASD in humans and loss of *Glra2* in mice causes early developmental defects of cortical neurons (Piton et al., 2011, Avila et al., 2013b, Avila et al., 2014, Iossifov et al., 2014, Pilorge et al., 2015). However, it remains unclear if embryonic defects resulting from loss of glycine signaling underlie ASD through poor cortical network maturation.

The present work explores the consequences of the embryonic loss of GlyR α2 homomers in the establishment of mature and functional cortical networks. We show a significant reduction of the number of INs and PNs residing in upper layers and layer V of postnatal *Glra2*KO mice. Furthermore, we demonstrate that cortical neurons of layer V have impaired dendrite and spine morphologies that are associated with synaptogenesis defects during cortical maturation. These morphological alterations are associated with functional defects that lead to a marked disruption of excitatory and inhibitory input-output of the cerebral cortex culminating in increased network excitability following treatment with 4 aminopyridine (4-AP) *in vitro.* In addition, *in vivo* experiments confirmed that adult *Glra2*KO mice show increased susceptibility to epileptic seizures after pentylenetetrazol (PTZ) injections.

Results

Genetic inactivation of Glra2 leads to reduced number of cortical neurons after birth

Glycine receptors composed of α2 subunits are widely distributed in the forebrain (Malosio et al., 1991). Previous work from our laboratory demonstrated that *Glra2*KO embryos have reduced number of PNs in several cortical layers and suffer from microcephaly (Avila et al., 2014). In addition, we showed that *Glra2* expression is required for proper migration of cortical INs from MGE to cerebral cortex (Avila et al., 2013b, Avila et al., 2014). At P7, *Glra2*KO animals showed a moderate microcephaly characterized by reduced brain weight and cerebral cortical wall thickness (Figures 1a-1b). This phenotype gradually toned down with age; it was less pronounced at P14 (Figures S1a-S1b) and not seen in adulthood (Pilorge et al., 2015). We next assessed the laminar composition of the cortex at P7 and P14 and observed less upper layer neurons expressing Cux1 (Figures 1c-S1c) as well as less $Ctip2^{+}$ (strong labeling) sub-cerebral PNs (mostly layer V) in *Glra2*KO mice, as compared to WT littermates (McKenna et al., 2011) (Figure 1d-S1d). Surprisingly, the number of cortico-thalamic PNs of layer VI, which co-express Tbr1 and Ctip2 (weak labeling) remained unchanged between genotypes (Figure 1d-S1d) (McKenna et al., 2011). We next assessed the population of cortical INs using a GFP reporter mouse line (Dlx5,6:Cre-IRES-EGFP, later mentioned as Dlx 5-6) that we crossed with *Glra2KO* mice. Dlx 5-6 INs represent 75-80% of the total population of cortical interneurons born in the MGE and caudal ganglionic eminences (CGE) (Marin, 2012). We observed an overall reduction of the number of GFP-expressing INs without layering alteration in the cerebral cortex of P7 and P14 *Glra2*KO mice, as compared to controls (Figures 2a-S1e). These results were comparable to those previously observed during embryogenesis (Avila et al., 2013b). The population of Dlx 5-6 INs deriving from the MGE mainly specializes into parvalbumin (PV) and somatostatin (SST) expressing interneurons (Marin, 2012). PV interneurons mostly target the soma of PNs and

are thought to control the synchrony of network gamma oscillations in the brain (Hu et al., 2014). On the other hand, SST interneurons innervate local PV interneurons, placing them in an ideal position to drive inhibition and directly mediate plasticity mechanisms via the inhibition of incoming information to the distal dendrites of pyramidal neurons (Silberberg and Markram, 2007, Hioki et al., 2013). While both number and layering distribution of SST-positive INs were similar in both genotypes at P7 and P14 (Figures 2b-S1f), immunolabelings of brain sections from P14 *Glra2*KO mice showed a 20% reduction of PV-expressing interneuron number without disruption of their layering (Figure 2c). Dlx 5-6 cells born in CGE predominantly specify into calretinin-positive (CR) interneurons, which inhibit INs and PNs by targeting soma and apical dendrites. During early postnatal development, most CR-positive INs settle in cortical layers II-III and few populate layer V. During adulthood, these neurons are widely distributed throughout the cortex (Barinka and Druga, 2010). Our results showed a significant reduction of the number of CR-expressing INs at P7 upon depletion of *Glra2* (Figure 2d).

Overall, the somatosensory cortex of *Glra2*KO mice is characterized by a quantitative reduction of both PNs and INs likely resulting from the proliferation and migration defects occurring during embryogenesis (Avila et al., 2013b, Avila et al., 2014). These data suggest a possible impairment of cortical network connectivity. For this purpose, we assessed the formation and activity of the *Glra2*KO mouse cortical neuronal network at late postnatal ages.

Morphological defects of layer V neurons in the cerebral cortex of Glra2KO animals

We performed reconstructions of biocytin-filled layer V PNs from P7 animals to assess their morphological development and spine density. Cellular identity was confirmed by morphological and electrophysiological characteristics (Christophe et al., 2005, Hattox and Nelson, 2007) (Figures 3a, 5a-b). We observed an increase of total dendritic length, which

was associated with more branching points (Figure 3a). Sholl analyses made separately on apical and basal dendrites revealed more distal branching of basal dendrites upon loss of *Glra2* while apical dendrite branching complexity was comparable between genotypes at P7 (Figure 3b). When assessed at the dendrite level, spine density of layer V neurons from *Glra2*KO mice was reduced both in basal (Figure 3c) and apical dendrites (data not shown). However, according to total dendritic length increase, the total number of spines (total dendritic length*spine density) per neuron was increased in *Glra2*KO mice, as compared to WT littermate (Figure 3c). In order to discriminate excitatory inputs at the level of dendritic shafts and spines, we monitored the expression of the post-synaptic protein PSD95 in biocytin filled layer V PNs dendrites. PSD95 is expressed in the shaft, dendritic spines and soma binding directly NMDA receptors via an integral PDZ domain (Kornau et al., 1995) and indirectly to AMPA receptors through stargazin (Bats et al., 2007). It has been reported that in brain slices or neuronal cortical cultures from young animals the excitatory input to the dendritic tree is unequally shared between spines (36%) and shaft (64%), whilst in adult synaptic connections occurred mainly at the level of spines (Boyer et al., 1998). We observed an overall increase of PSD95 boutons in the dendrites of *Glra2*KO layer V PNs (Figure 3d). Indeed, the percentage of PSD95 boutons was decreased in spines (38.00±1.67% in WT vs 23.6±1.62% in *Glra2*KO) and largely increased in shafts upon deletion of in *Glra2* (62.00±1.67% in WT vs 76.4±1.62% in *Glra2*KO) (data not shown). Such defects may indeed arise from the poor maturation of dendritic spines in *Glra2*KO layer V PNs as revealed by Golgi staining showing a significant increase of immature spines (filamentous) at the expense of mature spines (mushroom shaped) (Figure S2). Interestingly, the enrichment in filamentous spines alongside the increased branching is a common feature of several neurodevelopmental X-linked pathologies and epilepsy models (Irwin et al., 2000, Ma et al., 2013).

We subsequently analyzed the morphology of GFP^+ cortical INs to assess local circuitry defects in the layer V of *Glra2*KO mouse cortex. We thus performed morphological reconstructions of layer V fast-spiking INs (Figures 4a, 5d-e). The total dendritic length was increased and was associated with more complex branching upon loss of *Glra2* (Figure 4a). Sholl analyses confirmed the increased dendrite ramification of *Glra2KO* INs *(*Figure 4b). We further analyzed dendritic spines, which are present in several subtypes of INs in hippocampus and cortex (Kawaguchi et al., 2006). Our data showed reduced spine density in secondary dendrites as well as an increase of total number of dendritic spines per *Glra2KO* IN, as compared to WT IN (total dendritic length*spine density) (Figure 4c). Not only dendritic spines but also shafts correspond to sites of postsynaptic excitatory inputs on INs (Scheuss and Bonhoeffer, 2014), thus we analyzed the expression of PSD95 at the dendritic level of INs. We observed an increased density of PSD95 positive boutons in *Glra2*KO layer V INs (Figure 4d). Taken together, these experiments revealed branching and spinogenesis defects upon *Glra2* deletion for both PNs and INs that populate the layer V of the somatosensory cortex, further supporting possible alterations in their connections after birth.

Functional defects of layer V neurons in the cerebral cortex of postnatal Glra2KO mice

To test whether the dendritic alterations of layer V neurons impair their connections, we performed whole-cell patch-clamp recordings to measure spontaneous excitatory and inhibitory postsynaptic currents (sEPSCs and sIPSCs, respectively) at P7. Layer V PNs are either callosal (projecting within the cerebral cortex) or subcortical (targeting the thalamus, the midbrain, the hindbrain and the spinal cord) neurons. Here, we focused on P7 layer V subcortical PNs acting as main output from cortex to lower brain regions. At P7, these neurons are characterized by the extension of the apical dendrite into layer I with elaborated

apical tufts as well as by electrophysiological parameters (specific input resistance, membrane capacitance and resting potential) (Figure 3a-5a,b) (Koester and O'Leary, 1992, Christophe et al., 2005, Hattox and Nelson, 2007). Patch-clamp recordings revealed increased frequency of spontaneous postsynaptic currents (sPSCs) in layer V PNs that lack *Glra2* expression, as compared to WT PNs (Figure 5c). Moreover, after blocking sIPSCs by infusing $GABA_AR$ antagonists (10 μM gabazine or 10 μM bicuculline methiodide), we observed an increased frequency of sEPSCs in *Glra2*KO neurons (Figure 6a). Additionally, we calculated the charge transfer of the averaged sEPSCs as a measure of the membrane depolarizing capacity of the current. The averaged sEPSCs charge per event (670.7±184.1 fC in *Glra2*KO vs 289.2±55.9 fC in WT; p value<0.05) and charge transfer were significantly increased in *Glra2*KO, and were associated with a reduction in rise time in the *Glra2*KO layer V neurons at P7 compared to WT neurons (Figures 6a and S3a). In strike contrast, the frequency of sIPSCs - measured after addition of CNQX (5 μM) and AP5 (5 μM) - was significantly reduced in *Glra2*KO layer V PNs (Figure 6c). We also observed a correlated reduction of charge transfer of averaged sIPSCs due to the reduction of rise time and amplitude (Figures 6c and S3b). Infusion of 1μM of tetrodotoxin (TTX) blocked action potential-dependent events and allowed us to measure mini post-synaptic currents (mPSCs). Recordings made at P7 showed that *Glra2*KO layer V PNs had increased frequency of mEPSCs (*Glra2*KO 0.209±0.048 Hz versus WT 0.091±0.024 Hz n=6 and 6 p<0.05) and conversely, reduced frequency of mIPSCs, as compared to their controls (*Glra2*KO 0.073±0.020 Hz versus WT 0.262±0.073 Hz n=6 and 6 p<0.01) (data not shown).

To assess the local microcircuitry of layer V in *Glra2*KO mice, we evaluated the synaptic activity of GFP^+ INs. We thus selected fast-spiking GFP^+ INs (Daw et al., 2007, Hu et al., 2014, Yang et al., 2014) (Figure 5d-e) to analyze sEPSCs and sIPSCs at P7. *Glra2*KO INs showed more sPSCs, as compared to WT INs (Figure 5f). We recorded an increased

frequency of sEPSCs in presence of $GABA_AR$ antagonists in P7 *Glra2*KO INs as compared to their controls (Figure 7a). Measurements of the averaged sEPSCs charge per event (805.1±180.9 fC in *Glra2*KO vs 419.3±74.8 fC in WT; p value<0.05) and charge transfer showed a clear shift toward excitation for INs in *Glra2*KO mice, suggesting an overall increased membrane excitation (Figure 7a). These results were associated with a reduction of rise time and increased decay time (Figure S3c). On the other hand, the frequency of sIPSCs recorded after pharmacological addition of glutamatergic blockers (5 µM of CNQX and AP5) was significantly decreased upon genetic deletion of *Glra2* (Figure 7c). This reduction was associated with a decreased charge transfer in *Glra2*KO INs, as compared to controls, associated with an increased rise time and decay time (Figure 7c and S3d). mEPSCs were increased in *Glra2*KO INs (*Glra2*KO 0.278±0.065 Hz versus WT 0.1±0.034 Hz n=6 and 6 p<0.05), whilst mIPSCs were reduced in *Glra2*KO INs, as compared to control INs (*Glra2*KO 0.041±0.011 Hz versus WT 0.112±0.025 Hz n=6 and 6 p<0.05) (data not shown). The synaptic phenotype of *Glra2*KO layer V neurons did not result from compensation by other GlyR subunits (Figures S4-S5). Indeed, we found that the molecular composition of GlyRs was dynamically remodeled during the development in the somatosensory cortex (Figures S5a-S5f). The expression of α2 subunits predominated during embryonic development, while other GlyR subunits showed a progressive enrichment during mouse brain development. Moreover, layer V PNs and INs expressed functional extrasynaptic GlyRs at P7 in both WT and *Glra2*KO mice (Figures S4a-S4c). These receptors were tonically activated, as application of 1µM strychnine did not alter the frequency of sPSCs recorded in cortical neurons from both genotypes (Figure S4b-S4d). These results also supported previous observations made in prefrontal cerebral cortex PNs (Liu et al., 2014, Salling and Harrison, 2014).

The functional synaptic defects measured by patch-clamp recordings suggested impairment of both excitatory and inhibitory synapse densities. We thus analyzed the expression of specific excitatory (PSD95) and inhibitory (glutamic acid decarboxylase-65, or GAD65) synaptic markers at the perisomatic level of layer V GFP^+ INs and $Ctip2^+$ subcortical-targeting PNs. The analysis of P7 *Glra2*KO cortices revealed increased density of PSD95-expressing (Figures 6b and 7b) and reduced density of GAD65-expressing (Figures 6d and 7d) perisomatic boutons in both PNs and INs. Altogether, these data support a possible disruption of the balance between excitatory and inhibitory connections in neurons from layer V of the *Glra2*KO cortex of postnatal mice (Figures 8a-8b).

Genetic inactivation of Glra2 increases susceptibility to chemoconvulsant-induced epileptic seizures

The morphological and functional alterations observed in the layer V circuitry of *Glra2*KO mice suggest that they may be prone to seizures upon challenging conditions. To check this hypothesis, we performed *in vitro* recordings of adult layer V PNs in the presence of 4-AP, which enhances transmitter release at both inhibitory and excitatory terminals (Buckle and Haas, 1982), thus inducing network driven interictal-like discharge via the block of A- and D-type K^+ mediated currents (Traub et al., 1995). Layer V PNs recorded in adult mice never showed ictal discharge during bath application of 50 µM 4-AP (n=4 for both genotypes) (Figure 8c). Interestingly, at 100 µM 4-AP most layer V PNs recorded in *Glra2*KO mouse cortices exhibited ictal discharges as compared to WT (n=6 per genotype) (Figure 8c). Bath-perfusion of 500 µM 4-AP (n=3 per genotype) induced ictal activity and afterdischarge in both genotypes with an averaged time-to- ictal event (TTI, the interval between the beginning of stimulation with proconvulsant and the appearance of the ictal event) of 67±8.5 seconds for *Glra2*KO and 88.3±4.1 in WT adults (data not shown). Next, we compared the behavior of

adult *Glra2*KO and WT mice infused with PTZ, a chemoconvulsant used for seizure test (Loyens et al., 2012) (Figure 8d). Two types of motor seizures are elicited by PTZ: minimal seizures, restricted to forelimbs and predominantly clonic; and major seizures which consists of a generalized tonic-clonic response that contracts the muscles of the whole body leading to cramped tonic state (Depaulis et al., 1989). Specifically, PTZ was infused in the tail vein of *Glra2*KO and WT littermates in order to measure seizure thresholds. Depletion of *Glra2* significantly decreased PTZ thresholds for all the following mild and severe behaviors: ear twitch, myoclonic twitch, forelimb clonus, falling, tonic hindlimb extension (THE) and death (Figure 8d). The increased seizure susceptibility observed in *Glra2*KO mice treated with PTZ, suggests a critical role of α2 GlyRs for proper establishment of the cortical circuitry during brain maturation.

Discussion

Neurotransmitters belong to the microenvironment of neuronal progenitors and some act extrasynaptically to promote their maturation into functional neurons (Nguyen et al., 2001, Heng et al., 2007). We recently demonstrated that on the one hand, α2 GlyRs expressed at embryonic stages control neurogenesis and neuronal migration of cortical progenitors, thereby setting a stable basis for network construction (Avila et al., 2013b, Avila et al., 2014). Here we show that *Glra2*KO mice have moderate microcephaly at P7 and P14 that likely arises from a reduced production of PV- and CR-expressing INs, as well as PNs dedicated to most cortical layers. After birth, the α2 GlyRs remain expressed in the cerebral cortex (Becker et al., 1993, Young-Pearse et al., 2006), suggesting they might modulate cortical network maturation and homeostasis. In this work, we present evidence indicating that functional GlyR α2 homomers control the morphological differentiation and functional integration of layer V neurons and interneurons into the cortical network. Absence of *Glra2* led to the formation of cortical network prone to over-excitability, as further supported by the higher susceptibility of *Glra2*KO mice to epileptic seizures induced by PTZ tail infusion, as compared to WT littermates.

Our data suggest a critical role for α2 GlyRs in the fine control of branching and synaptogenesis of cortical PNs and fast spiking INs of layer V at P7. Both neuronal populations displayed an increase of dendritic complexity and total number of spines in the cortex of P7 *Glra2*KO mice, as compared to WT littermates (Figure 8a and 8b). It is noteworthy that the dendritic field and the spines undergo significant changes in shape and number in response to neuronal activity (Yuste and Bonhoeffer, 2004). Thus, the branching phenotype that we observed in layer V neurons of *Glra2*KO may partly be cell autonomous and result from loss of glycinergic signaling in layer V neurons and partly non-cell

autonomous as a result of disturbed synaptic input from upstream neurons onto layer V neurons.

Accumulation of morphological defects in cortical neurons upon *Glra2* inactivation lead to alterations in synaptic communication. The overall reduction of inhibitory synaptic efficacy (INs to INs and INs to PNs) is paralleled by an increased excitatory synaptic activity of the PNs to PNs and PNs to INs. Glutamatergic neurons form multiple synapses onto INs and PNs at somatic and dendritic level. In the INs, glutamatergic synapses typically form clusters on a small fraction of dendrites, whilst these synapses are widespread and highly innervate PNs (Buhl et al., 1997). The present work reports an increased number of excitatory synapses at the dendrites and soma of both PNs and INs from *Glra2*KO mice, as compared to WT littermates (Figures 8a and 8b). Such defects may lead to a global modification of the output balance toward excitation in both PNs and INs. Although an increased excitation of INs might result in increased inhibitory input on PNs, the decreased number of INs in layer V probably counteract the effect of the increased inhibition at the single IN level. According to the decreased rheobase and increased excitatory charge transfer (Figure 5b and 6a), *Glra2*KO layer V PNs are likely more excitable as compared to their WT controls. Together, our results support an alteration of synaptogenesis of cortical neurons in postnatal *Glra2*KO mice, leading to an increase in the global output of layer V neurons of the cerebral cortex.

The physiological consequences of a modified excitation/inhibition balance in cortical network may underlie epilepsy. We thus investigated the epileptiform activity in the cortical circuitry of *Glra2* KO mice at the cellular level using bath application of 4-AP (Avoli and Olivier, 1989, Tasker et al., 1992), or *in vivo* after tail vein infusion of the chemoconvulsant PTZ (Loyens et al., 2012). Here, we report higher susceptibility to lower concentration of 4-AP-induced interictal-like discharges in PNs of the layer V recorded in brain slices from adult *Glra2*KO mice suggesting a higher susceptibility to epileptic brain activity. Moreover, the *in*

vivo experiments showed that lower PTZ doses are required to trigger the typical seizure-related behaviors in *Glra2*KO mice, as compared to WT littermates, supporting an increased susceptibility to epileptic seizures upon inactivation of *Glra2*.

Three recent studies showed genetic anomalies in the *Glra2* gene associated with ASD in humans (Piton et al., 2011, Iossifov et al., 2014, Pilorge et al., 2015). Loss of function of α2 GlyRs impaired synaptic plasticity and social and cognitive impairments (Pilorge et al., 2015). The disrupted excitation-inhibition balance of layer V circuits reported in the present work may account for the etiology of ASD as well as comorbid epilepsy. In general, epilepsy is a common condition occurring in up to 30% of the ASD patients, especially those with intellectual disabilities confirming the link with cortical anomalies (Lai et al., 2014). Furthermore, the idea of a connection between genetic modification of GlyRs and epilepsy has already been proposed by several *in vitro* and clinical studies. *In vitro* studies have demonstrated that glycine depresses cell-bursting activity in the hippocampus under hyperexcitable conditions via GlyR activation (Chattipakorn and McMahon, 2003). This was consistent with the idea that activation of GlyRs is required to suppress the generation of epileptiform discharges in the hippocampus of young rats (Chattipakorn and McMahon, 2003, Song et al., 2006, Chen et al., 2014). Finally, some mutations of GlyR subunit-coding genes have been associated with epilepsy in human (Eichler et al., 2009, Epi and Epilepsy Phenome/Genome, 2013, Pilorge et al., 2015).

In summary, our results demonstrate a physiological role for α2 GlyRs during cortical network formation and homeostasis. Moreover, we suggest that disruption of *Glra2* expression in humans might lead to cortical neuronal migration as well as maturation defects that increased susceptibility to epileptic seizures.

Materials and methods

Animals. All animal experimental procedures were performed following guidelines of local ethical committees at Hasselt and Liège Universities as well as at the Vrije Universiteit Brussel. *Glra2*KO mice (Avila et al., 2013b) were backcrossed onto the MF1 background, and some were crossed with Dlx5,6:Cre-IRES-EGFP (Stenman et al., 2003) for selected experiments and housed at the BIOMED Institute animal facility. C57BL/6J *Glra2*KO mice were used for behavioral experiments after confirmation of similar defects in the cerebral cortex as the MF1 mouse line for *Glra2*KO.

Immunohistochemistry. Postnatal day 7 and 14 mice were transcardially perfused with PBS followed by 4% PFA in PBS and post-fixed by immersion in the same fixative overnight at 4°C. Brains were cut in 20 µm slices for all experiments. Primary antibodies in this study include the following: goat anti-Cux1 (1:25; Sc-6327, Santa Cruz Biotechnologies, USA), rat anti-Ctip2 (1:200; ab18465, Abcam, UK), rabbit anti-Tbr1 (1:200; ab31940, Abcam, UK), mouse anti-PV (1:500, MAB 1572, Millipore, USA), mouse anti-calretinin (1:1000, mab1568, Millipore) rat anti-somatostatin (1:50, mab354, Millipore, USA), mouse anti-GAD65 (1:20; Developmental studies hybridoma bank, USA), rabbit anti-PSD95 (1:100; ab18258, Abcam, UK), mouse anti-NeuN clone A60 (1:100, Millipore, USA), rabbit anti-NeuN (1:100, Millipore) and rabbit anti-GFP (1:200; ab6556, Abcam, UK). Specific secondary antibodies Alexa 488, 555 and 647 (A555, A647 and A488, Life Technologies, Belgium) were used.

Electrophysiology. PNs and GFP^+ INs of somatosensory cortex in the layer V were identified by morphological, electrophysiological criteria and expression of GFP. Localization of layer V was visually obtained by recognition of barrel somatosensory cortex. Whole-cell patch-clamp recordings were performed using an Heka EPC9 (Heka elektronik, Germany) patch-clamp amplifier. All experiments were carried out at room temperature, in voltage-clamp mode at a holding voltage equal to -60 mV. All ligands and blockers were either bath applied

or focally applied. The internal solution was composed by KCl 130, NaCl 5, $CaCl_2$ 1, $MgCl_2$ 1, Hepes 10, EGTA 10, NaATP 2, NaGTP 0.5 (mM) and 5% biocytin (pH adjusted to 7.3 with KOH) whilst the external artificial cerebrospinal fluid (ACSF) solution was composed by NaCl 125, KCl 2.5, $MgCl_2$ 1, $CaCl_2$ 2, $NaHCO_3$ 25, NaH_2PO_4 1.25, Glucose 25 for P7 mice and 10 for adult mice (mM). Spontaneous post-synaptic currents (sPSCs) were obtained by 2 minutes recordings of spontaneous events. To detect sIPSCs 5 µM 6-cyano-7-nitroquinoxaline-2,3-dione, CNQX (C239, Sigma, Belgium), and 5 µM (2R)-amino-5-phosphonovaleric acid, AP5 (A8054, Sigma, Belgium), were added to the bath before recording. To detect sEPSCs 10 µM of bicuculline methiodide (14343, Sigma, Belgium) was added to the ACSF. This was confirmed using also 10 µM gabazine (S106, Sigma, Belgium), isomer of bicuculline. After 5 minutes of bath perfusion in order to allow the drugs to be effective, 2 minutes recordings were measured. Experimental approach to detect mPSCs was equivalent as the sPSCs with addition of 1 µM of TTX (Alomone labs, Belgium) for the bath perfusion. Charge transfer (Q) was calculated by integrating the area under the PSC waveform. The mean PSC synaptic current was calculated as the charge transfer of either the averaged sEPSC or sIPSCs multiplied by mean PSC frequency (current × frequency, in femto-Coulomb/sec. ($fCxs^{-1}$).

Electrophysiological properties were evaluated and evoked by 10 currents step injection from 0 pA to 100 pA in 10 pA increments.

The amplitude of glycine-elicited currents was assessed by brief and focal applications of 100 µM glycine that lasted for 5 seconds. Distance of 150-200 µm from the surface of the slice was used for focal application using a Warner perfusion system that allowed an exchange time of less than 20 ms (Fast-Step, Warner Instrument Corp.). Evaluation of presence of synaptic GlyRs was assessed using 5 µM CNQX (C239, Sigma, Belgium), 5 µM AP5

(A8054, Sigma), 10 µM of bicuculline methiodide (14343, Sigma, Belgium) and 1 µM strychnine (S0532 Sigma, Belgium) in a similar approach used for the sPSCs.

For the ictal discharge induction, action potentials were measured during subsequently 5 minutes control in ACSF, 5 minutes in 50, 100 or 500 µM bath applied 4-aminopyridine (4-AP, Abcam, UK) and a 15 minutes recovery in ACSF.

Data acquisition was performed using Patchmaster (Heka elektronik) and analyzed using pClamp (Molecular Devices, USA) and Clampfit (Molecular Devices) software for glycine elicited currents and current-clamp experiments. MiniAnalysis (Synaptosoft, Inc., USA) was used for synaptic currents.

Herpes virus mediated gene transfer. The 450-bp DLX I12b enhancer (Potter et al., 2009) was inserted into the LT HSV vector (Fenno et al., 2014), replacing the hCMV promoter and thereby generating the following transcriptional cassette: Dlx I12b-GFP-WPRE-poly(A) site. The Dlx vector was packaged into virus using the amplicon method (Neve and Lim, 2013). The titer of the virus preparation was 3.5 x 10^8 infectious units (i.u.)/ml. Slices from P7 mice were removed from recording chamber and infected for 1-3 days. Slices were fixed overnight in 4% PFA and then stained with rabbit anti-PSD95 (1:100; ab18258, Abcam, UK).

Seizure induction. Male *Glra2*KO mice and their wild-type littermates (+/- 12 weeks) were used to determine seizure thresholds, based on the pentylenetetrazol (PTZ)-induced stereotyped seizure behavior. The threshold for the different phases of PTZ-induced seizure activity was determined by infusing a solution containing 7.5 mg/ml of PTZ (Sigma Chemical Company, St. Louis, MO, USA) with 5000 IE/mL heparin dissolved in 0.9% NaCl solution. The infusion was injected through a 29G needle, attached to polyethylene tubing (Smiths, Keene, USA) and inserted into the tail vein of the animals at a constant rate of 150 µl/min, using a Hamilton syringe mounted to an infusion pump (CMA, Microdialysis, Solna,

Sweden). The animals were allowed to move freely in a cage made of plexiglas. The following endpoints were used to determine the seizure threshold: (1) ear twitch; (2) myoclonic twitch; (3) forelimb clonus, (4) clonus with loss of righting reflexes (falling); (5) THE; (6) death. Time was measured from the start of the PTZ infusion until the onset of these stages. The seizure thresholds were individually determined for each animal according to the following equation: dose (mg/kg) = duration of infusion (s) × rate of infusion (ml/min) × drug concentration (mg/ml) × 1000/(60 s × weight of mouse (g)).

Neuronal reconstruction. PNs and GFP-expressing INs of the layer V were filled with biocytin via the patch pipette and the 300 µm slices were fixed in 4% PFA for 1-2 hours. Reconstruction and semi-automated analysis of dendrite morphology, spines and bouton density were performed *in silico*. Biocytin-filled PNs and INs were reconstructed using Neuromantic (freeware software by Myatt, D.R.) which was used to calculated branching points and total dendritic length. Sholl analyses was performed by using Fiji Image J plug-in and analyzed using the linear method (Schindelin et al., 2012, Ferreira et al., 2014)

Cell counting and spine density. All cellular quantifications were performed in the brightest single plane along the Z-stack. Analysis of cell counts was carried out using the manual cell counter tool included ImageJ. Fiji Image J plugin was used to measure single dendrite length and count dendritic spines throughout the Z-stack.

Statistics. All data are expressed as mean ± standard error of the mean (SEM). Mean and error calculations, as well as statistical analyses were computed in GraphPad (GraphPad Software, Inc). Paired and unpaired t-test were used after Shapiro-Wilk normality test, while two-way Anova with Bonferroni post hoc test was used for Sholl analysis, bin percentages of cells and developmental qPCR for GlyRs.

Supplemental information: Supplemental Information includes eight figures and Supplemental experimental Procedures and can be found with this article online

References

Avila A, Nguyen L, Rigo JM. 2013a. Glycine receptors and brain development. Frontiers in cellular neuroscience 7:184.

Avila A, Vidal PM, Dear TN, Harvey RJ, Rigo JM, Nguyen L. 2013b. Glycine Receptor alpha2 Subunit Activation Promotes Cortical Interneuron Migration. Cell reports 4:738-750.

Avila A, Vidal PM, Tielens S, Morelli G, Laguesse S, Harvey RJ, Rigo JM, Nguyen L. 2014. Glycine receptors control the generation of projection neurons in the developing cerebral cortex. Cell death and differentiation.

Avoli M, Olivier A. 1989. Electrophysiological properties and synaptic responses in the deep layers of the human epileptogenic neocortex in vitro. Journal of neurophysiology 61:589-606.

Barinka F, Druga R. 2010. Calretinin expression in the mammalian neocortex: a review. Physiological research / Academia Scientiarum Bohemoslovaca 59:665-677.

Bats C, Groc L, Choquet D. 2007. The interaction between Stargazin and PSD-95 regulates AMPA receptor surface trafficking. Neuron 53:719-734.

Becker CM, Betz H, Schroder H. 1993. Expression of inhibitory glycine receptors in postnatal rat cerebral cortex. Brain research 606:220-226.

Betz H, Laube B. 2006. Glycine receptors: recent insights into their structural organization and functional diversity. Journal of neurochemistry 97:1600-1610.

Boyer C, Schikorski T, Stevens CF. 1998. Comparison of hippocampal dendritic spines in culture and in brain. The Journal of neuroscience : the official journal of the Society for Neuroscience 18:5294-5300.

Buckle PJ, Haas HL. 1982. Enhancement of synaptic transmission by 4-aminopyridine in hippocampal slices of the rat. The Journal of physiology 326:109-122.

Buhl EH, Tamas G, Szilagyi T, Stricker C, Paulsen O, Somogyi P. 1997. Effect, number and location of synapses made by single pyramidal cells onto aspiny interneurones of cat visual cortex. The Journal of physiology 500 (Pt 3):689-713.

Chattipakorn SC, McMahon LL. 2003. Strychnine-sensitive glycine receptors depress hyperexcitability in rat dentate gyrus. Journal of neurophysiology 89:1339-1342.

Chen R, Okabe A, Sun H, Sharopov S, Hanganu-Opatz IL, Kolbaev SN, Fukuda A, Luhmann HJ, Kilb W. 2014. Activation of glycine receptors modulates spontaneous epileptiform activity in the immature rat hippocampus. The Journal of physiology 592:2153-2168.

Christophe E, Doerflinger N, Lavery DJ, Molnar Z, Charpak S, Audinat E. 2005. Two populations of layer v pyramidal cells of the mouse neocortex: development and sensitivity to anesthetics. Journal of neurophysiology 94:3357-3367.

Daw MI, Ashby MC, Isaac JT. 2007. Coordinated developmental recruitment of latent fast spiking interneurons in layer IV barrel cortex. Nature neuroscience 10:453-461.

Depaulis A, Snead OC, 3rd, Marescaux C, Vergnes M. 1989. Suppressive effects of intranigral injection of muscimol in three models of generalized non-convulsive epilepsy induced by chemical agents. Brain research 498:64-72.

Eichler SA, Forstera B, Smolinsky B, Juttner R, Lehmann TN, Fahling M, Schwarz G, Legendre P, Meier JC. 2009. Splice-specific roles of glycine receptor alpha3 in the hippocampus. The European journal of neuroscience 30:1077-1091.

Epi KC, Epilepsy Phenome/Genome P. 2013. De novo mutations in epileptic encephalopathies. Nature 501:217-221.

Fenno LE, Mattis J, Ramakrishnan C, Hyun M, Lee SY, He M, Tucciarone J, Selimbeyoglu A, Berndt A, Grosenick L, Zalocusky KA, Bernstein H, Swanson H, Perry C, Diester I, Boyce FM, Bass CE, Neve R, Huang ZJ, Deisseroth K. 2014. Targeting cells with single vectors using multiple-feature Boolean logic. Nature methods 11:763-772.

Ferreira TA, Blackman AV, Oyrer J, Jayabal S, Chung AJ, Watt AJ, Sjostrom PJ, van Meyel DJ . 2014. Neuronal morphometry directly from bitmap images. Nature methods 11:982-984.

Flint AC, Liu X, Kriegstein AR. 1998. Nonsynaptic glycine receptor activation during early neocortical development. Neuron 20:43-53.

Geschwind DH, Rakic P. 2013. Cortical evolution: judge the brain by its cover. Neuron 80:633-647.
Greig LC, Woodworth MB, Galazo MJ, Padmanabhan H, Macklis JD . 2013. Molecular logic of neocortical projection neuron specification, development and diversity. Nature reviews Neuroscience 14:755-769.
Harris KD, Mrsic-Flogel TD. 2013. Cortical connectivity and sensory coding. Nature 503:51-58.
Hattox AM, Nelson SB. 2007. Layer V neurons in mouse cortex projecting to different targets have distinct physiological properties. Journal of neurophysiology 98:3330-3340.
Heng JI, Moonen G, Nguyen L. 2007. Neurotransmitters regulate cell migration in the telencephalon. The European journal of neuroscience 26:537-546.
Hioki H, Okamoto S, Konno M, Kameda H, Sohn J, Kuramoto E, Fujiyama F, Kaneko T. 2013. Cell type-specific inhibitory inputs to dendritic and somatic compartments of parvalbumin-expressing neocortical interneuron. The Journal of neuroscience : the official journal of the Society for Neuroscience 33:544-555.
Hu H, Gan J, Jonas P. 2014. Interneurons. Fast-spiking, parvalbumin(+) GABAergic interneurons: from cellular design to microcircuit function. Science 345:1255263.
Huang ZJ. 2014. Toward a genetic dissection of cortical circuits in the mouse. Neuron 83:1284-1302.
Huttenlocher PR. 1979. Synaptic density in human frontal cortex - developmental changes and effects of aging. Brain research 163:195-205.
Huttenlocher PR, Dabholkar AS. 1997. Regional differences in synaptogenesis in human cerebral cortex. The Journal of comparative neurology 387:167-178.
Iossifov I, O'Roak BJ, Sanders SJ, Ronemus M, Krumm N, Levy D, Stessman HA, Witherspoon KT, Vives L, Patterson KE, Smith JD, Paeper B, Nickerson DA, Dea J, Dong S, Gonzalez LE, Mandell JD, Mane SM, Murtha MT, Sullivan CA, Walker MF, Waqar Z, Wei L, Willsey AJ, Yamrom B, Lee YH, Grabowska E, Dalkic E, Wang Z, Marks S, Andrews P, Leotta A, Kendall J, Hakker I, Rosenbaum J, Ma B, Rodgers L, Troge J, Narzisi G, Yoon S, Schatz MC, Ye K, McCombie WR, Shendure J, Eichler EE, State MW, Wigler M. 2014. The contribution of de novo coding mutations to autism spectrum disorder. Nature 515:216-221.
Irwin SA, Galvez R, Greenough WT. 2000. Dendritic spine structural anomalies in fragile-X mental retardation syndrome. Cerebral cortex 10:1038-1044.
Kawaguchi Y, Karube F, Kubota Y. 2006. Dendritic branch typing and spine expression patterns in cortical nonpyramidal cells. Cerebral cortex 16:696-711.
Koester SE, O'Leary DD. 1992. Functional classes of cortical projection neurons develop dendritic distinctions by class-specific sculpting of an early common pattern. The Journal of neuroscience : the official journal of the Society for Neuroscience 12:1382-1393.
Kornau HC, Schenker LT, Kennedy MB, Seeburg PH. 1995. Domain interaction between NMDA receptor subunits and the postsynaptic density protein PSD-95. Science 269:1737-1740.
Lai MC, Lombardo MV, Baron-Cohen S . 2014. Autism. Lancet 383:896-910.
Lee KS, Schottler F, Collins JL, Lanzino G, Couture D, Rao A, Hiramatsu K, Goto Y, Hong SC, Caner H, Yamamoto H, Chen ZF, Bertram E, Berr S, Omary R, Scrable H, Jackson T, Goble J, Eisenman L. 1997. A genetic animal model of human neocortical heterotopia associated with seizures. The Journal of neuroscience : the official journal of the Society for Neuroscience 17:6236-6242.
Lewis DA, Levitt P. 2002. Schizophrenia as a disorder of neurodevelopment. Annual review of neuroscience 25:409-432.
Liu Y, Huang D, Wen R, Chen X, Yi H. 2014. Glycine receptor-mediated inhibition of medial prefrontal cortical pyramidal cells. Biochemical and biophysical research communications.
Loyens E, Vermoesen K, Schallier A, Michotte Y, Smolders I. 2012. Proconvulsive effects of oxytocin in the generalized pentylenetetrazol mouse model are mediated by vasopressin 1a receptors. Brain research 1436:43-50.
Lui JH, Hansen DV, Kriegstein AR. 2011. Development and evolution of the human neocortex. Cell 146:18-36.
Ma Y, Ramachandran A, Ford N, Parada I, Prince DA. 2013. Remodeling of dendrites and spines in the C1q knockout model of genetic epilepsy. Epilepsia 54:1232-1239.
Malosio ML, Marqueze-Pouey B, Kuhse J, Betz H. 1991. Widespread expression of glycine receptor subunit mRNAs in the adult and developing rat brain. The EMBO journal 10:2401-2409.

Marin O. 2012. Interneuron dysfunction in psychiatric disorders. Nature reviews Neuroscience 13:107-120.

McKenna WL, Betancourt J, Larkin KA, Abrams B, Guo C, Rubenstein JL, Chen B. 2011. Tbr1 and Fezf2 regulate alternate corticofugal neuronal identities during neocortical development. The Journal of neuroscience : the official journal of the Society for Neuroscience 31:549-564.

Molyneaux BJ, Arlotta P, Menezes JR, Macklis JD. 2007. Neuronal subtype specification in the cerebral cortex. Nature reviews Neuroscience 8:427-437.

Neve RL, Lim F . 2013. Generation of high-titer defective HSV-1 vectors. Current protocols in neuroscience / editorial board, Jacqueline N Crawley [et al] Chapter 4:Unit 4 13.

Nguyen L, Rigo JM, Rocher V, Belachew S, Malgrange B, Rogister B, Leprince P, Moonen G. 2001. Neurotransmitters as early signals for central nervous system development. Cell and tissue research 305:187-202.

Pilorge M, Fassier C, Le Corronc H, Potey A, Bai J, De Gois S, Delaby E, Assouline B, Guinchat V, Devillard F, Delorme R, Nygren G, Rastam M, Meier JC, Otani S, Cheval H, James VM, Topf M, Dear TN, Gillberg C, Leboyer M, Giros B, Gautron S, Hazan J, Harvey RJ, Legendre P, Betancur C. 2015. Genetic and functional analyses demonstrate a role for abnormal glycinergic signaling in autism. Molecular psychiatry.

Piton A, Gauthier J, Hamdan FF, Lafreniere RG, Yang Y, Henrion E, Laurent S, Noreau A, Thibodeau P, Karemera L, Spiegelman D, Kuku F, Duguay J, Destroismaisons L, Jolivet P, Cote M, Lachapelle K, Diallo O, Raymond A, Marineau C, Champagne N, Xiong L, Gaspar C, Riviere JB, Tarabeux J, Cossette P, Krebs MO, Rapoport JL, Addington A, Delisi LE, Mottron L, Joober R, Fombonne E, Drapeau P, Rouleau GA. 2011. Systematic resequencing of X-chromosome synaptic genes in autism spectrum disorder and schizophrenia. Molecular psychiatry 16:867-880.

Potter GB, Petryniak MA, Shevchenko E, McKinsey GL, Ekker M, Rubenstein JL . 2009. Generation of Cre-transgenic mice using Dlx1/Dlx2 enhancers and their characterization in GABAergic interneurons. Molecular and cellular neurosciences 40:167-186.

Rakic P . 2009. Evolution of the neocortex: a perspective from developmental biology. Nature reviews Neuroscience 10:724-735.

Rakic P, Bourgeois JP, Goldman-Rakic PS. 1994. Synaptic development of the cerebral cortex: implications for learning, memory, and mental illness. Progress in brain research 102:227-243.

Represa A, Ben-Ari Y . 2005. Trophic actions of GABA on neuronal development. Trends in neurosciences 28:278-283.

Ruediger T, Bolz J . 2007. Neurotransmitters and the development of neuronal circuits. Advances in experimental medicine and biology 621:104-115.

Salling MC, Harrison NL. 2014. Strychnine-sensitive glycine receptors on pyramidal neurons in layers II/III of the mouse prefrontal cortex are tonically activated. Journal of neurophysiology 112:1169-1178.

Scheuss V, Bonhoeffer T. 2014. Function of dendritic spines on hippocampal inhibitory neurons. Cerebral cortex 24:3142-3153.

Schindelin J, Arganda-Carreras I, Frise E, Kaynig V, Longair M, Pietzsch T, Preibisch S, Rueden C, Saalfeld S, Schmid B, Tinevez JY, White DJ, Hartenstein V, Eliceiri K, Tomancak P, Cardona A. 2012. Fiji: an open-source platform for biological-image analysis. Nature methods 9:676-682.

Silberberg G, Markram H. 2007. Disynaptic inhibition between neocortical pyramidal cells mediated by Martinotti cells. Neuron 53:735-746.

Song W, Chattipakorn SC, McMahon LL. 2006. Glycine-gated chloride channels depress synaptic transmission in rat hippocampus. Journal of neurophysiology 95:2366-2379.

Sorensen SA, Bernard A, Menon V, Royall JJ, Glattfelder KJ, Desta T, Hirokawa K, Mortrud M, Miller JA, Zeng H, Hohmann JG, Jones AR, Lein ES . 2013. Correlated Gene Expression and Target Specificity Demonstrate Excitatory Projection Neuron Diversity. Cerebral cortex.

Stenman J, Toresson H, Campbell K. 2003. Identification of two distinct progenitor populations in the lateral ganglionic eminence: implications for striatal and olfactory bulb neurogenesis. The Journal of neuroscience : the official journal of the Society for Neuroscience 23:167-174.

Tasker JG, Peacock WJ, Dudek FE . 1992. Local synaptic circuits and epileptiform activity in slices of neocortex from children with intractable epilepsy. Journal of neurophysiology 67:496-507.
Traub RD, Colling SB, Jefferys JG. 1995. Cellular mechanisms of 4-aminopyridine-induced synchronized after-discharges in the rat hippocampal slice. The Journal of physiology 489 (Pt 1):127-140.
Valiente M, Marin O. 2010. Neuronal migration mechanisms in development and disease. Current opinion in neurobiology 20:68-78.
Yang JM, Zhang J, Yu YQ, Duan S, Li XM. 2014. Postnatal development of 2 microcircuits involving fast-spiking interneurons in the mouse prefrontal cortex. Cerebral cortex 24:98-109.
Young-Pearse TL, Ivic L, Kriegstein AR, Cepko CL. 2006. Characterization of mice with targeted deletion of glycine receptor alpha 2. Molecular and cellular biology 26:5728-5734.
Yuste R, Bonhoeffer T . 2004. Genesis of dendritic spines: insights from ultrastructural and imaging studies. Nature reviews Neuroscience 5:24-34.

Figure Legends

Figure 1. *Genetic disruption of Glra2 results in microcephaly and reduction in cortical thickness.* **a**, low magnification *Glra2*KO images showing reduction of brain size (scale bar 1000 μm) correlated with a decrease in brain weight in P7 *Glra2*KO mouse as compared to WT control. Values are expressed as mean ± SEM, n=7 WT and 7 *Glra2*KO P7 mice; *p<0.05, t-test. **b**, cortical thickness at P7 in *Glra2*KO mice in dorsal (D), dorsolateral (D-L) and lateral (L) somatosensory cortex (scale bar 500 μm). Values are expressed as mean ± SEM, n=7 WT and 7 *Glra2*KO P7 mice; *p<0.05, **p<0.01, t-test. **c-d,** immunolabelings performed on brain section showing cells expressing Cux1 (green, **c**) Ctip2 (red, **d**), Tbr1 (green, **d**) and the nuclear label Dapi (blue, **d**) in P7 WT or *Glra2*KO mice (scale bar 100 μm). Layer II/III and V PNs are significantly decreased at P7, while layer VI do not show difference between genotypes. Values are expressed as mean ± SEM, n=20 WT and 20 *Glra2*KO brain sections taken from 6 brains per genotype; **p<0.01, ***p<0.001, t-test.

Figure 2. *Genetic deletion of Glra2 results in reduction of different subtype of INs within the cerebral cortex.* **a**, immunolabelings for Dlx 5-6 GFP^+ INs at P7 showing overall reduction of INs without major differences in redistribution through division of cortex in bins of equal size (scale bar 100 μm). Values are expressed as mean ± SEM, n=12 WT and 12 *Glra2*KO taken from 3 brains per genotype; **p<0.01; t-test and two-way Anova with Bonferroni post hoc tests for bins division. **b**, immunolabeling for somatostatin INs (red, SST) and nuclear staining Dapi (blue) in P7 somatosensory cortices showing no differences in number and distribution between WT and *Glra2*KO (scale bar 100 μm). Values are expressed as mean ± SEM, n=12 WT and 12 *Glra2*KO taken from 3 brains per genotype; t-test and two-way Anova with Bonferroni post hocs for bins division. **c**, immunolabelings performed on brain section showing INs expressing parvalbumin (red, PV) and the nuclear label Dapi (blue) in P14 WT or *Glra2*KO mice (scale bar 100 μm). No major redistribution was observed, but overall reduction in *Glra2*KO mice. Values are expressed as mean ± SEM, n=16 WT and 16 *Glra2*KO brain sections taken from 4 brains per genotype ***p<0.001, t-test and two-way Anova with Bonferroni post hoc tests for bins division. **d**, immunolabeling for calretinin INs (red, CR) in P7 brain

showing a reduction in number in the *Glra2*KO mice (scale bar 100 μm). Values are expressed as mean ± SEM, n=12 WT and 12 *Glra2*KO taken from 3 brains per genotype; **p<0.01, t-test.

Figure 3. *Morphological defects of layer V PNs at P7.* **a**, reconstruction of biocytin-filled P7 layer V PNs showing increase in total dendritic length and branching points in *Glra2*KO mice (scale bar 100 μm). Values are expressed as mean ± SEM, n=11 WT and 8 *Glra2*KO P7 mice; **p<0.01, t-test. **b**, Sholl analyses of apical dendrites (top) and basal dendrites (bottom) of layer V PNs (scale bars 50 μm). Values are expressed as mean ± SEM, n=11 WT and 8 *Glra2*KO P7 mice; *p< 0.05, **p<0.01, ***p<0.001, two-way Anova with Bonferroni post hocs. **c**, spine density on basal dendrites of layer V PNs at P7 displaying a decrease in spine density in *Glra2*KO mice at P7 (scale bar 1 μm). Total number of spines was calculated as follow: total dendritic length × spine density). Values are expressed as mean ± SEM, n=11 WT and 8 *Glra2*KO P7 mice; *p<0.05, t-test. **d**, PSD95 (red) bouton density at the level of dendrites of biocytin- filled PNs of the layer V (green) at P7 (scale bar 1 μm). Values are expressed as mean ± SEM, n=10 WT and 10 *Glra2*KO neurons from 3 animals per genotype; *p< 0.05; t-test.

Figure 4. *Morphological defects of layer V GFP$^+$ INs at P7.* **a**, reconstruction of biocytin-filled P7 GFP$^+$ INs of the layer V showing increase of total dendritic length and branching points in *Glra2*KO mice (scale bar 100 μm). Values are expressed as mean ± SEM, n=12 WT and 15 *Glra2*KO P7 mice; *p<0.05, t-test. **b**, Sholl analyses of GFP$^+$ INs. Dendrites show increased branching complexity at the dendrites of *Glra2*KO mice (scale bar 50 μm). Values are expressed as mean ± SEM, n=12 WT and 15 *Glra2*KO P7 mice; *p< 0.05, **p<0.01, ***p<0.001, two-way Anova with Bonferroni post hoc test. **c**, spine density on dendrites of GFP$^+$ INs of the layer V at P7 displaying a decrease of spine density in *Glra2*KO mice (scale bar 1 μm). Total number of spines was calculated as follow: total dendritic length × spine density. Values are expressed as mean ± SEM, n=12 WT and 15 *Glra2*KO P7 mice; *p<0.05, t-test. **d**, PSD95 (red) bouton density representing shafts at the level of dendrites of Dlx1 GFP$^+$ INs (green) at P7 (scale bar 1 μm). Values are expressed as mean ± SEM, n=15 WT and 15 *Glra2*KO neurons from 3 animals per genotype; ***p<0.001; t-test.

Figure 5. *Spontaneous post-synaptic currents and electrophysiological parameters of layer V PNs and GFP$^+$INs in acute P7 brain slices.* **a**, representative traces and action potential firing of neurons projecting to subcortical area of the brain in the layer V at P7 in WT and *Glra2*KO mice (scale bar 10 mV,100 ms). Electrophysiological properties were evaluated and evoked by 10 currents step injection from 0 pA to 100 pA in 10 pA increments. No difference was observed in firing rate as showed with 50 pA injection. **b**, table representing electrophysiological parameters of layer V PNs. Capacitance is significantly increased in *Glra2*KO PNs (**p<0.01), while rheobase is reduced in the *Glra2*KO PNs (* p<0.05). Values are expressed as mean ± SEM, n=56 for WT and n=38 for *Glra2*KO neurons used for several electrophysiological approaches. **c**, representative traces of spontaneous post-synaptic currents obtained in layer V PNs in ACSF showing increase in frequency in *Glra2*KO neurons (scale bar 32 pA, 10 s). Close up picture shows representative traces of single event displaying defect in rise time 10-90% and amplitude but not decay time (scale bar is 20 pA, 50 ms). Values are expressed as mean ± SEM, n=56 for WT and n=38 for *Glra2*KO neurons used for several electrophysiological approaches; * p<0.05, ** p<0.01, *** p<0.001; t-test. **d**, representative traces and action potential firing of GFP$^+$ INs with fast-spiking behavior in the layer V at P7 in WT and *Glra2*KO mice (scale bar 10 mV, 100 ms). Electrophysiological properties were evaluated and evoked by 10 currents step injection from 0 pA to 100 pA in 10 pA increments. No difference was observed in firing rate as showed with 30 pA injection. **e**, table representing electrophysiological parameters of layer V GFP$^+$ INs. Capacitance and input resistance are significantly increased in *Glra2*KO INs (respectively *p<0.05 and **p<0.01), while rheobase is decreased in *Glra2*KO INs (***p<0.01); n=25 for WT and n=31 for *Glra2*KO interneurons. Values are expressed as mean ± SEM. **f**, representative traces of spontaneous post-synaptic currents obtained in layer V INs obtained in ACSF showing increase in frequency in *Glra2*KO INs (scale bar 32 pA, 10 s). Close up picture showing of single event displaying defect in rise time 10-90% but not decay time and amplitude (scale bar is 20 pA, 50 ms). Values are expressed as mean ± SEM, n=25 for WT and n=31 for *Glra2*KO interneurons; *p<0.05; t-test.

Figure 6. *Glra2 deletion leads to alteration of synaptic activity of layer V projection neurons.* Whole-cell patch-clamp analyses performed on layer V PNs in acute P7 brain slices. **a**, representative traces

of excitatory post-synaptic currents obtained in layer V PNs after bath application of 10 μM bicuculline showing increase in frequency in *Glra2*KO neurons (scale bar 32 pA, 10 s). Magnifications show representative traces of single event displaying defect in charge transfer (fC/s) (scale bar 10 pA, 50 ms). Values are expressed as mean ± SEM, n=24 WT and 17 *Glra2*KO neurons taken from at least 10 mice per genotype; *p<0.05, **p<0.01; t-test. **b**, triple immunolabeling performed on P7 brain section showing layer V PNs expressing Ctip2 (bottom panels, violet), NeuN (top panel, green) and excitatory postsynaptic marker PSD95 (top panel, red) (scale bar 10 μm). Density of PSD95 perisomatic boutons was manually counted showing an increase in *Glra2*KO mice. Values are expressed as mean ± SEM, n=30 WT and 30 *Glra2*KO neurons from 3 animals per genotype; ***p<0.001; t-test. **c**, representative traces of inhibitory post-synaptic currents obtained in layer V PNs after bath application of 5 μM CNQX and 5 μM AP5 showing decrease in frequency in *Glra2*KO neurons (scale bar 32 pA, 10 s). Zoomed pictures show representative traces of single event displaying charge transfer defect (fC/s) (scale bar 10 pA, 50 ms). Values are expressed as mean ± SEM, n=46 WT and 21 *Glra2*KO cells from at least 10 animals per genotype; *p<0.05; t-test. **d**, triple immunolabeling performed on P7 brain section showing layer V PNs expressing Ctip2 (bottom panels, violet), NeuN (top panel, green) and inhibitory marker GAD65 (top panel, red) (scale bar 10 μm). Density of GAD65 perisomatic boutons was manually counted showing a decrease in *Glra2*KO mice. Values are expressed as mean ± SEM, n=30 WT and 30 *Glra2*KO neurons from 3 animals per genotype; ***p<0.001; t-test.

Figure 7. *Glra2 disruption leads to alteration of synaptic activity of layer V GFP$^+$ INs.* Whole-cell patch-clamp analyses performed on layer V GFP$^+$ INs in acute P7 brain slices. **a**, representative traces of excitatory post-synaptic currents obtained in layer V GFP$^+$ INs after bath application of 10 μM bicuculline showing increase in frequency in *Glra2*KO neurons (scale bar 32 pA, 10 s). Magnified picture showing a representative traces of single event displaying charge transfer defect (fC/s) (scale bar 10 pA, 50 ms). Values are expressed as mean ± SEM, n=18 WT and 19 *Glra2*KO INs from at least 10 mice per genotype; *p<0.05; t-test. **b**, double immunolabeling performed on P7 brain section showing layer V GFP$^+$ INs (green) and excitatory postsynaptic marker PSD95 (red) (scale bar 10 μm).

Density of PSD95 perisomatic boutons was manually counted showing an increase in *Glra2*KO mice. Values are expressed as mean ± SEM, n=30 WT and 30 *Glra2*KO neurons from 3 animals per genotype; ***p<0.001; t-test. **c**, representative traces of inhibitory post-synaptic currents obtained in layer V GFP^+ INs after bath application of 5 μM CNQX and 5 μM AP5 showing decrease in frequency in *Glra2*KO INs (scale bar 32 pA, 10 s). Magnifications show representative traces of single event displaying defect in charge transfer (fC/s) (scale bar is 10 pA, 50 ms). Values are expressed as mean ± SEM, n=22 WT and 31 *Glra2*KO INs from at least 10 mice per genotype; *p<0.05; t-test. **d**, double immunolabeling performed on P7 brain section showing layer V GFP^+ INs (green) and inhibitory marker GAD65 (red) (scale bar 10 μm). Density of GAD65 perisomatic boutons was manually counted showing a decrease in *Glra2*KO mice. Values are expressed as mean ± SEM, n=30 WT and 30 *Glra2*KO neurons from 3 animals per genotype; ***p<0.001; t-test.

Figure 8. *Genetic targeting of Glra2 induces increased susceptibility to drug-induced epilepsy.* **a,** summary scheme illustrating cortical synaptic defects in the layer V of the cerebral cortex of WT or *Glra2*KO pups. PNs of layer V (green) present more ramification and total number of spines, despite the spine density appears to be reduced for each dendrite. Same pattern of morphology appears in layer V INs (red). Reduction in number of PNs of upper layers (blue), layer V (green) and overall number of INs (grey and red) occurs in the cerebral cortex of *Glra2*KO mice. These defects leads to less inhibitory input to PNs and INs while an increase in excitatory inputs to PNs and INs. **b**, table representing all morphological and functional defects occurring in PNs and INs of the layer V at P7. **c**, representative traces of 100 μM 4-AP bath application in adult WT or *Glra2*KO showing more susceptibility to 4-AP-induced ictal discharges in depletion upon *Glra2* (scale 10 mV, 1 min), n=4 per group for 50 μM, n=6 per group 100 μM and n=3 per group 500 μM. **d**, histogram of the typical seizure-related behavioral alterations following PTZ in adult WT and *Glra2*KO showing a higher susceptibility to epileptic seizures induced by PTZ in *Glra2*KO adult mice (THE= tonic hind limb extension). Values are expressed as mean ± SEM, n=12 WT and 11 *Glra2*KO mice, not all mice showed forelimb clonus n=7 WT and 8 *Glra2*KO mice ;*p<0.05, ***p<0.001; t-test

Funding:

This work was supported by several funding. B.B. and JM. R. are funded by Fonds Wetenschappelijk Onderzoek – Vlaanderen (FWO; G0A0513) and the Belgian Science Policy (IAP-VII network P7/10). L.N. is Research Associate from the Belgian National Funds for Scientific Research (F.R.S- F.N.R.S.). L.N. is funded by grants from the F.R.S.-F.N.R.S., the Fonds Léon Fredericq, the Fondation Simone et Pierre Clerdent, the Fondation Médicale Reine Elisabeth, the Belgian Science Policy (IAP-VII network P7/20), and the Actions de Recherche Concertées (ARC11/16-01). RJH is funded by the Medical Research Council (G0500833). Some scientific projects in the Nguyen laboratory are funded by the Walloon Excellence in Life Sciences and Biotechnology (WELBIO). The authors declare no competing financial interests.

Acknowledgments

We thank Dr. K. Campbell (University of Cincinnati, USA) for providing the Dlx5,6:Cre-GFP mouse line, and Neil T. Dear (South Australian Health and Medical Research Institute, Australia) for providing the *Glra2* knockout mouse line. The antibody against GAD65 was developed by Dr. David I. Gottlieb, and was obtained from the Developmental Studies Hybridoma Bank developed under the auspices of the NICHD and maintained at The University of Iowa, Department of Biology, Iowa City, IA 52242.

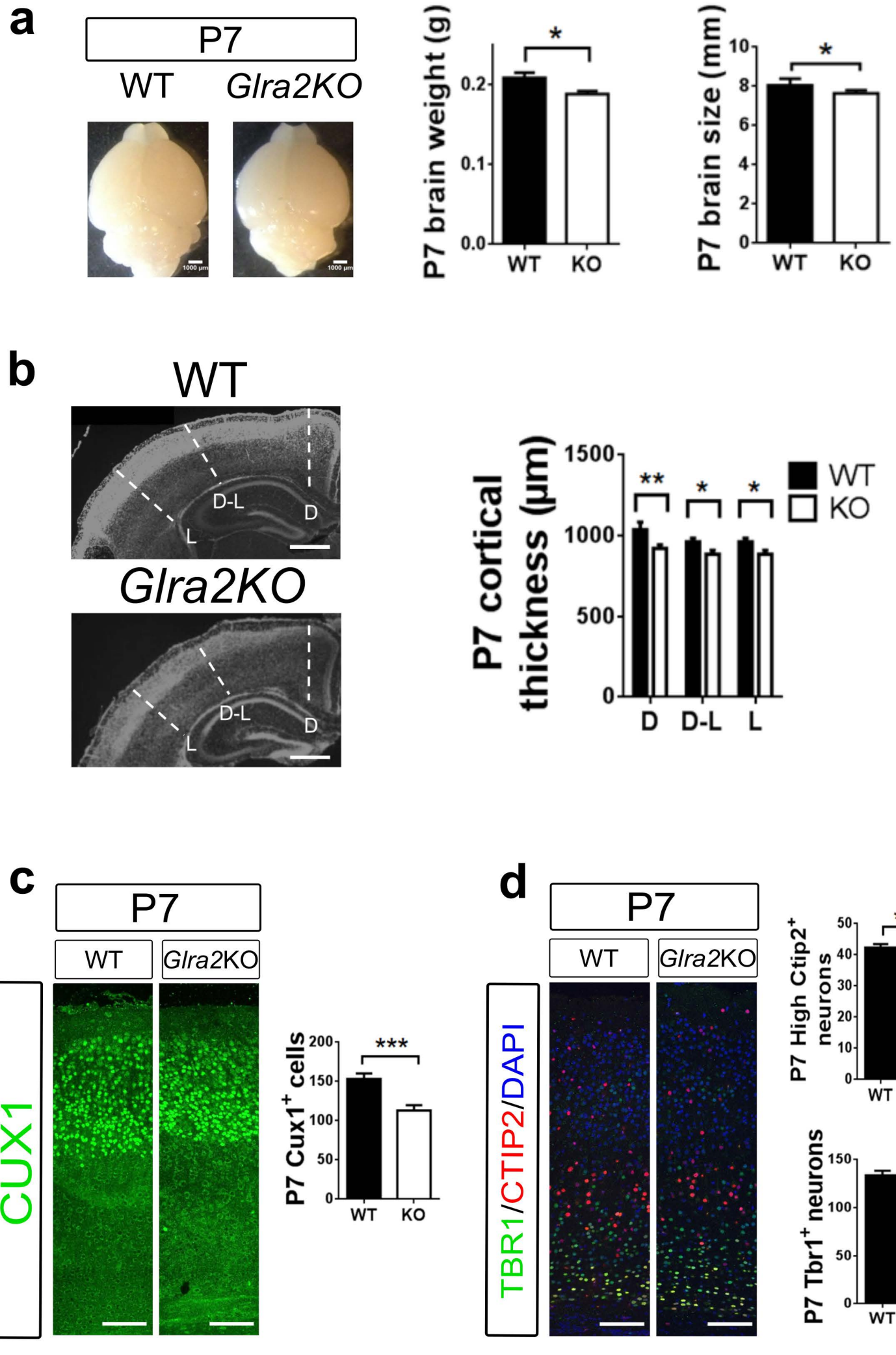
a
P7
WT
Glra2KO
1000 µm
1000 µm
P7 brain weight (g)
0.0
0.1
0.2
*
WT
KO
P7 brain size (mm)
0
2
4
6
8
10
*
WT
KO
b
WT
D-L
D
L
Glra2KO
D-L
D
L
P7 cortical thickness (µm)
0
500
1000
1500
**
*
*
WT
KO
D
D-L
L
c
P7
WT
Glra2KO
CUX1
P7 Cux1+ cells
0
50
100
150
200
***
WT
KO
d
P7
WT
Glra2KO
TBR1/CTIP2/DAPI
P7 High Ctip2+ neurons
0
10
20
30
40
50
**
WT
KO
P7 Tbr1+ neurons
0
50
100
150
WT
KO

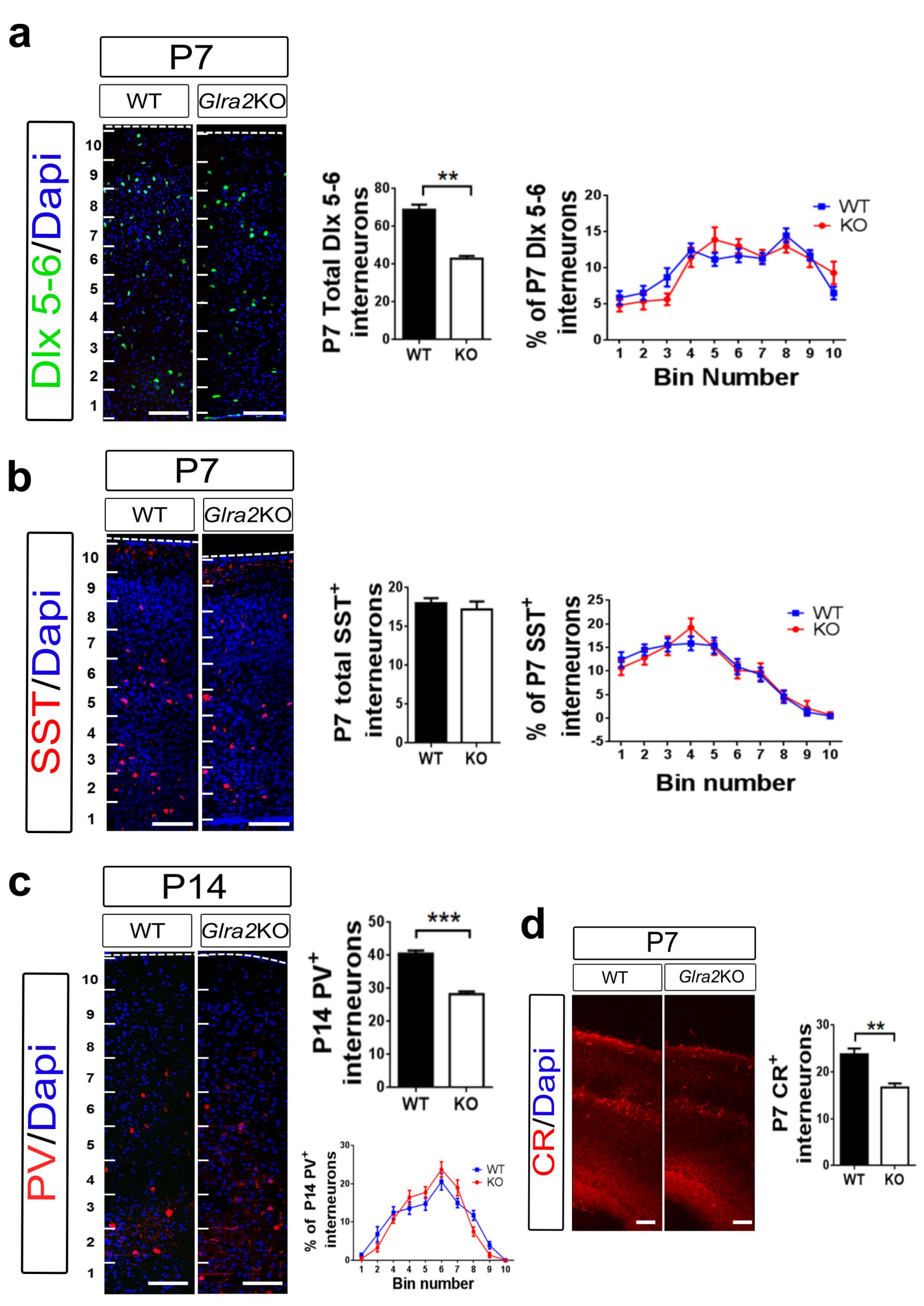
a
P7
WT
Glra2KO
Dlx 5-6/Dapi
10
9
8
7
6
5
4
3
2
1
P7 Total Dlx 5-6 interneurons
**
80
60
40
20
0
WT
KO
% of P7 Dlx 5-6 interneurons
20
15
10
5
0
1 2 3 4 5 6 7 8 9 10
Bin Number
WT
KO
b
P7
WT
Glra2KO
SST/Dapi
10
9
8
7
6
5
4
3
2
1
P7 total SST+ interneurons
20
15
10
5
0
WT
KO
% of P7 SST+ interneurons
25
20
15
10
5
0
-5
1 2 3 4 5 6 7 8 9 10
Bin number
WT
KO
c
P14
WT
Glra2KO
PV/Dapi
10
9
8
7
6
5
4
3
2
1
P14 PV+ interneurons
***
50
40
30
20
10
0
WT
KO
% of P14 PV+ interneurons
30
20
10
0
1 2 4 4 5 6 7 8 9 10
Bin number
WT
KO
d
P7
WT
Glra2KO
CR/Dapi
P7 CR+ interneurons
**
30
20
10
0
WT
KO

Figure 3

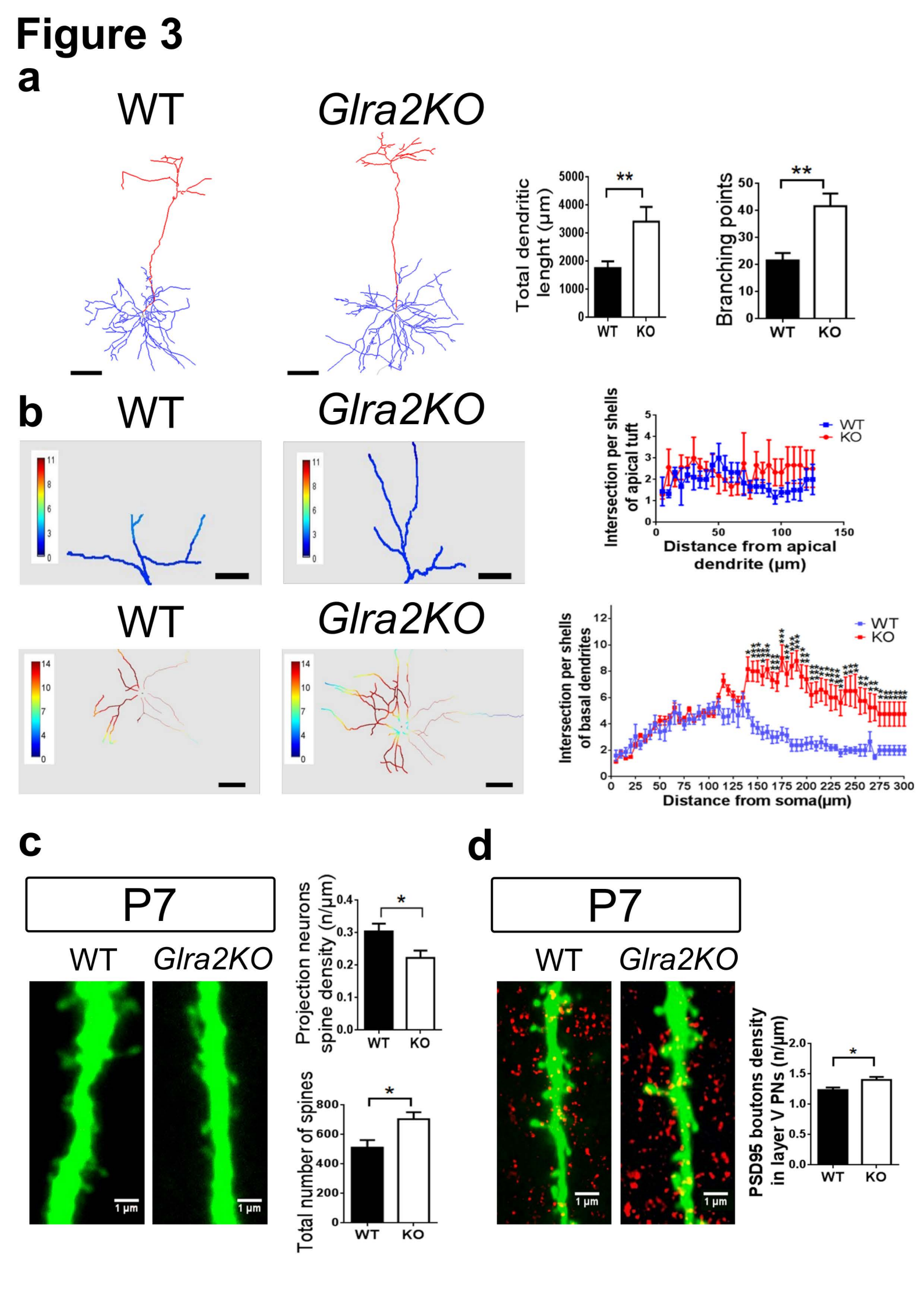
a
WT
Glra2KO
Total dendritic lenght (µm)
Branching points
WT
KO
b
WT
Glra2KO
Intersection per shells of apical tuft
Distance from apical dendrite (µm)
WT
Glra2KO
Intersection per shells of basal dendrites
Distance from soma(µm)
c
P7
WT
Glra2KO
Projection neurons spine density (n/µm)
Total number of spines
1 µm
d
P7
WT
Glra2KO
PSD95 boutons density in layer V PNs (n/µm)
1 µm

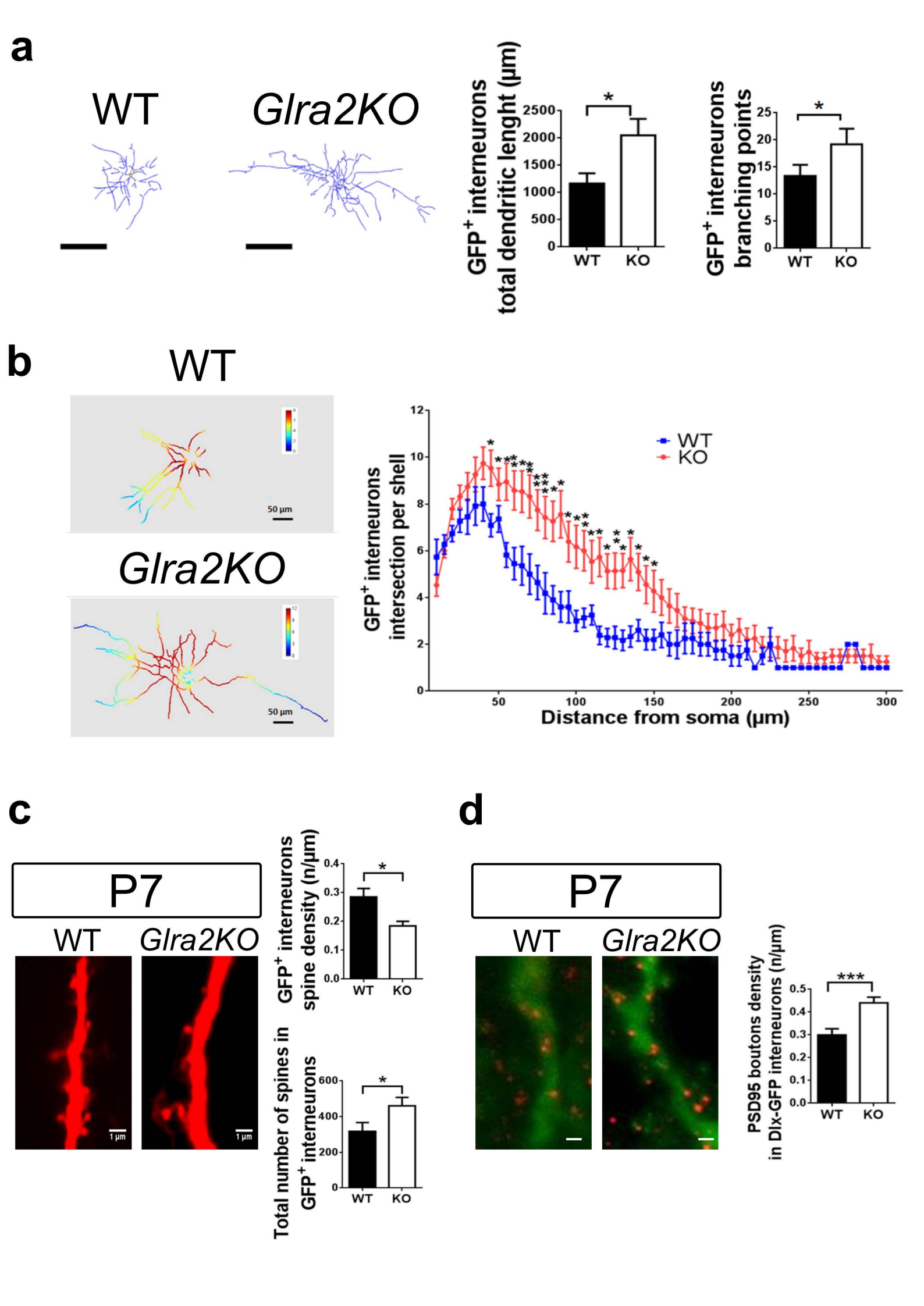
a
WT
Glra2KO
GFP+ interneurons total dendritic lenght (µm)
2500
2000
1500
1000
500
0
*
WT
KO
GFP+ interneurons branching points
25
20
15
10
5
0
*
WT
KO
b
WT
50 µm
Glra2KO
50 µm
GFP+ interneurons intersection per shell
12
10
8
6
4
2
0
WT
KO
50
100
150
200
250
300
Distance from soma (µm)
c
P7
WT
Glra2KO
1 µm
1 µm
GFP+ interneurons spine density (n/µm)
0.4
0.3
0.2
0.1
0.0
*
WT
KO
Total number of spines in GFP+ interneurons
600
400
200
0
*
WT
KO
d
P7
WT
Glra2KO
PSD95 boutons density in Dlx-GFP interneurons (n/µm)
0.5
0.4
0.3
0.2
0.1
0.0
***
WT
KO

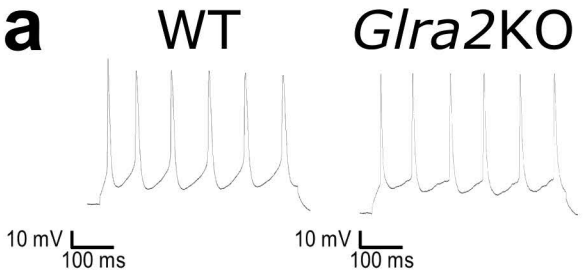

b

Projection neurons	Input resistance (mΩ)	Resting potential(mV)	Capacitance (pF)	Rheobase (pA)
WT	312.3 ± 14.5	-62.7 ± 1.1	80.77± 2.9	29.7±2.9
*Glra2*KO	304.9 ± 19.9	-64.9 ± 1.0	99.56 ± 5.7	18.7±2.7

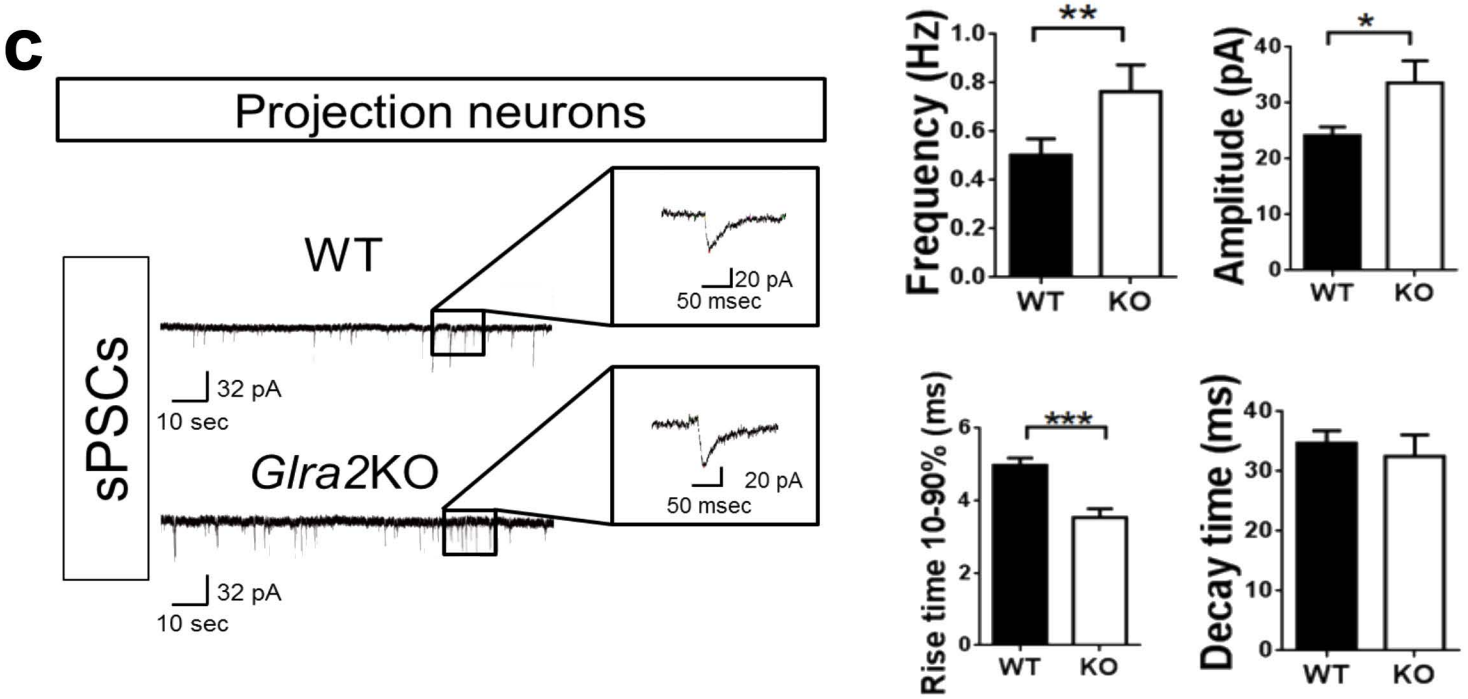

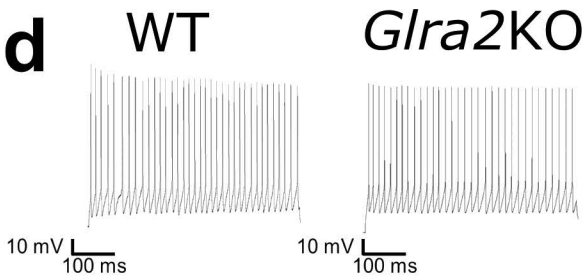

e

GFP⁺ interneurons	Input resistance (mΩ)	Resting potential (mV)	Capacitance (pF)	Rheobase (pA)
WT	298.8 ± 21.0	-63.1 ± 1.4	48.4 ± 3.2	35.2±4.9
*Glra2*KO	390.7 ± 31.4	-61.0 ± 2.0	60.5 ± 5.2	11.4±3.7

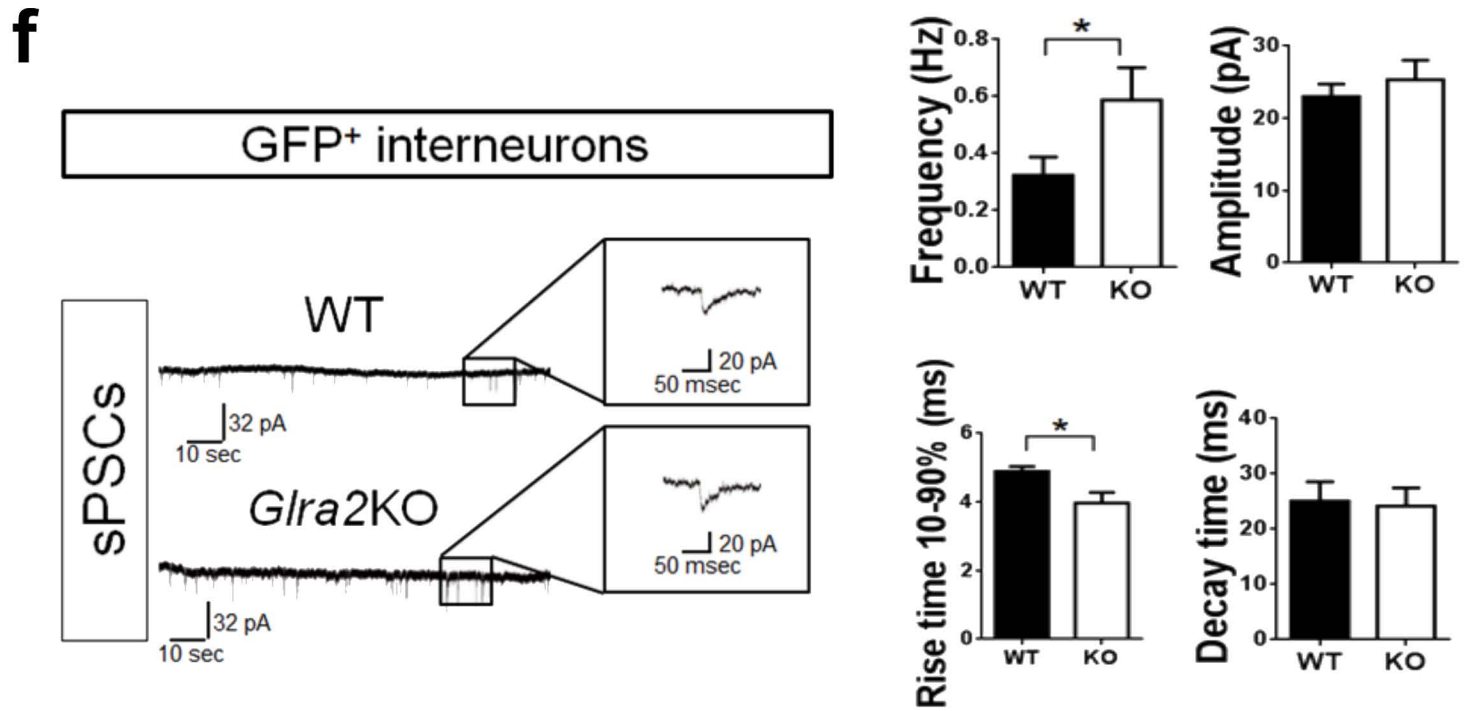

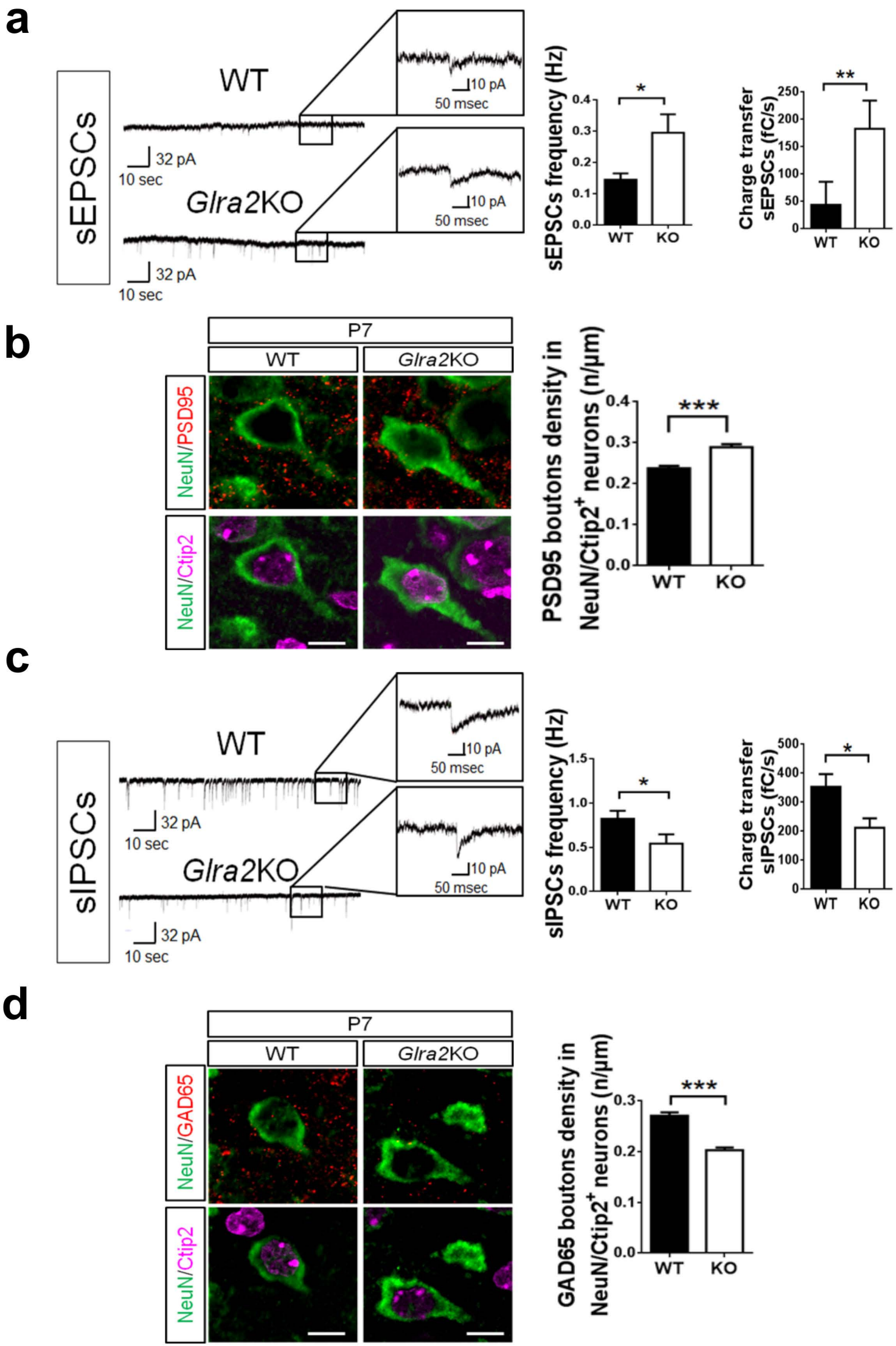
a
sEPSCs
WT
10 pA
50 msec
32 pA
10 sec
Glra2KO
10 pA
50 msec
32 pA
10 sec
sEPSCs frequency (Hz)
0.4
0.3
0.2
0.1
0.0
*
WT
KO
Charge transfer sEPSCs (fC/s)
250
200
150
100
50
0
**
WT
KO
b
P7
WT
Glra2KO
NeuN/PSD95
NeuN/Ctip2
PSD95 boutons density in NeuN/Ctip2+ neurons (n/µm)
0.4
0.3
0.2
0.1
0.0
***
WT
KO
c
sIPSCs
WT
10 pA
50 msec
32 pA
10 sec
Glra2KO
10 pA
50 msec
32 pA
10 sec
sIPSCs frequency (Hz)
1.5
1.0
0.5
0.0
*
WT
KO
Charge transfer sIPSCs (fC/s)
500
400
300
200
100
0
*
WT
KO
d
P7
WT
Glra2KO
NeuN/GAD65
NeuN/Ctip2
GAD65 boutons density in NeuN/Ctip2+ neurons (n/µm)
0.3
0.2
0.1
0.0
***
WT
KO

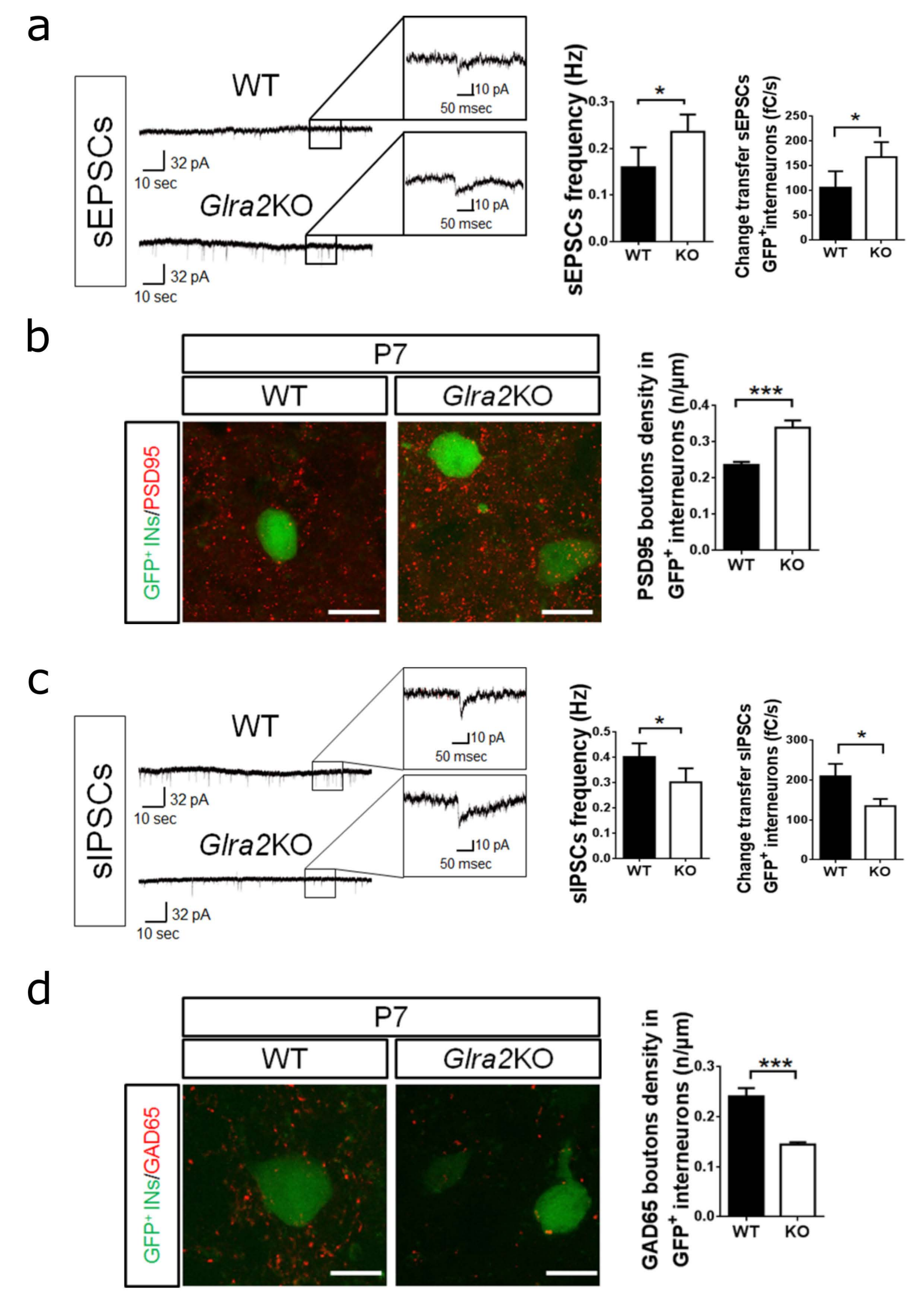
a
sEPSCs
WT
10 pA
50 msec
32 pA
10 sec
Glra2KO
10 pA
50 msec
32 pA
10 sec
sEPSCs frequency (Hz)
0.3
0.2
0.1
0.0
*
WT
KO
Change transfer sEPSCs GFP+interneurons (fC/s)
250
200
150
100
50
0
*
WT
KO
b
P7
WT
Glra2KO
GFP+ INs/PSD95
PSD95 boutons density in GFP+ interneurons (n/µm)
0.4
0.3
0.2
0.1
0.0
***
WT
KO
c
sIPSCs
WT
10 pA
50 msec
32 pA
10 sec
Glra2KO
10 pA
50 msec
32 pA
10 sec
sIPSCs frequency (Hz)
0.5
0.4
0.3
0.2
0.1
0.0
*
WT
KO
Change transfer sIPSCs GFP+ interneurons (fC/s)
300
200
100
0
*
WT
KO
d
P7
WT
Glra2KO
GFP+ INs/GAD65
GAD65 boutons density in GFP+ interneurons (n/µm)
0.3
0.2
0.1
0.0
***
WT
KO

a

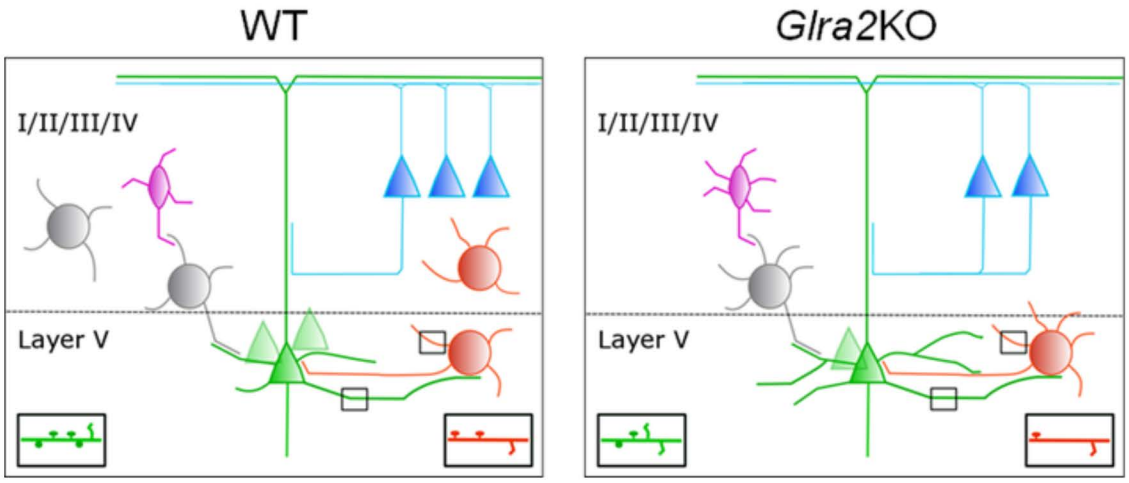

b

***Glra2*KO**	N cells	branches	spines	sEPSCs	sIPSCs	Excitatory synaptic density	Inhibitory synaptic density
PNs	↓ II-IV/V	↑	↑	↑	↓	↑	↓
INs	↓PV/CR	↑	↑	↑	↓	↑	↓

c

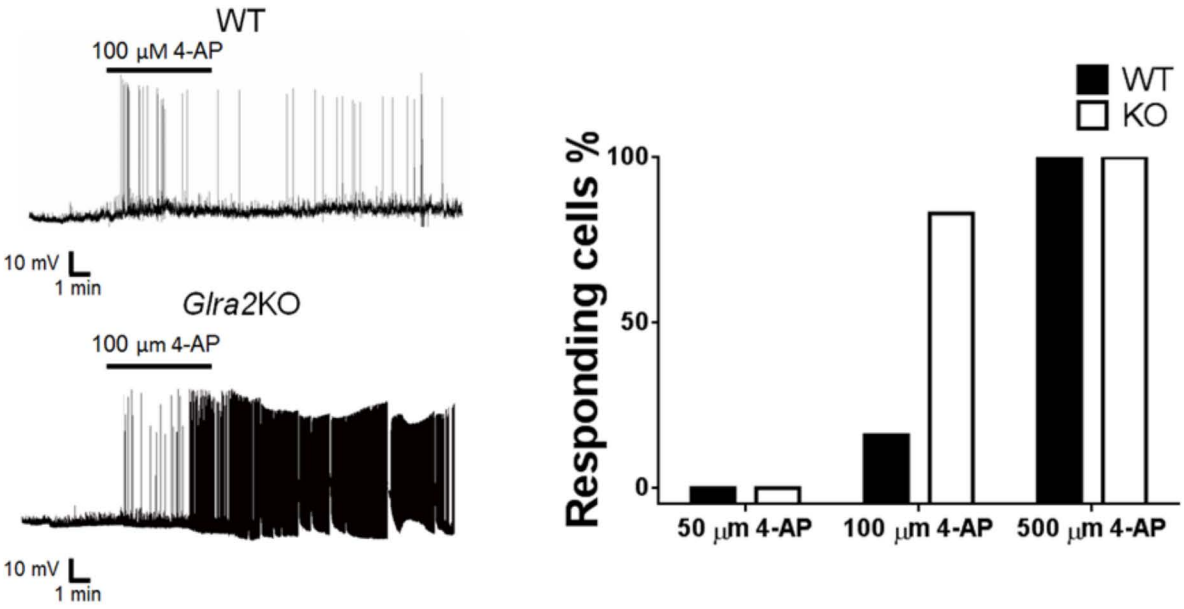

d

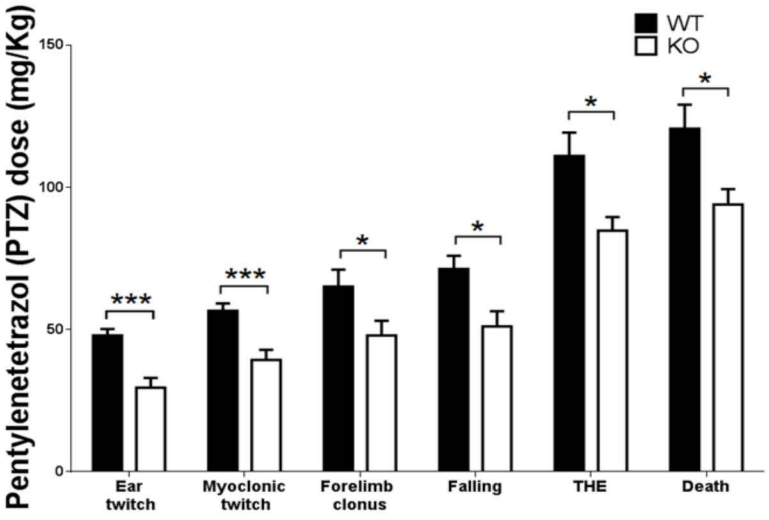

Supplemental figure and legends

Figure S1. *Gross morphological and cellular defects of P14 Glra2*KO *mice.* **a**, low magnification illustration of microcephaly at P14 in *Glra2*KO mice showing reduction of brain size (scale bar 1000 μm) correlated with a decrease in brain weight. Values are expressed as mean ± SEM, n=7 for each genotype, *Glra2*KO P14 mice; *p<0.05, t-test. **b**, representation of reduction of cortical thickness at P14 in *Glra2*KO mice in dorsal (D), dorsolateral (D-L) and lateral (L) somatosensory cortex (scale bar 500 μm). Values are expressed as mean ± SEM, n=7 for each genotype, *Glra2*KO P14 mice; *p<0.05, t-test. **c-d,** immunolabelings performed on brain section showing cells expressing Cux1 (green, **c**) Ctip2 (red, **d**), Tbr1 (green, **d**) and the nuclear label Dapi (blue, **d**) in P14 WT or *Glra2*KO mice (scale bar 100 μm). Layer II/III and V PNs are significantly decreased at P14, while layer VI do not show difference between genotypes. Values are expressed as mean ± SEM, n=20 WT and 20 *Glra2*KO brain sections taken from 6 brains per genotype; *p<0.05, **p<0.01, t-test. **e**, immunolabelings for Dlx 5-6 GFP^+ INs at P14 showing overall reduction of INs without major differences in redistribution through division of cortex in bins of equal size (scale bar 100 μm). Values are expressed as mean ± SEM, n=12 WT and 12 *Glra2*KO taken from 3 brains per genotype; *p<0.05; t-test and two-way Anova with Bonferroni post hoc tests for bins division. **f**, immunolabeling for somatostatin INs (red, SST) and nuclear staining Dapi (blue) in P14 somatosensory cortices showing no differences in number and distribution between WT and *Glra2*KO (scale bar 100 μm). Values are expressed as mean ± SEM, n=12 WT and 12 *Glra2*KO taken from 3 brains per genotype; t-test and two-way Anova with Bonferroni post hocs for bins division.

Figure S2. *Golgi staining for layer V PNs dendritic spine density and distribution at P7 in Glra2*KO *mice.* Representative picture of layer V PNs dendritic spines at P7 in *Glra2*KO mice showing decreased spine density and altered percentage of distribution of mushroom and filamentous but not of stub spines (scale bar 1 μm). Values are expressed as mean ± SEM, n=5 for each genotype at P7; *p<0.05, ***p<0.001, t-test.

Figure S3. *Rise time, decay time and amplitude of layer V PNs and GFP$^+$INs in Glra2KO at P7.* **a**, graphs representing the rise time, decay time and amplitude for sEPSCs showing a decrease in rise time 10-90% of layer V PNs in *Glra2*KO. Values are expressed as mean ± SEM, n=24 WT and 17 *Glra2*KO neurons; **p<0.01; t-test. **b**, graphs representing the rise time, decay time and amplitude for sIPSCs showing a decrease in rise time 10-90% and amplitude of layer V PNs in *Glra2*KO. Values are expressed as mean ± SEM, n=46 WT and 21 *Glra2*KO neurons; *p<0.05; t-test. **c**, graphs representing the rise time, decay time and amplitude for sEPSCs showing a decrease in rise time 10-90% and increase in decay time of layer V GFP$^+$ INs in *Glra2*KO. Values are expressed as mean ± SEM, n=18 WT and 19 *Glra2*KO neurons; *p<0.05; t-test. **d**, graphs representing the rise time, decay time and amplitude for sIPSCs showing an increase in rise time 10-90% and in decay time of layer V GFP$^+$ INs in *Glra2*KO. Values are expressed as mean ± SEM, n=18 WT and 19 *Glra2*KO neurons; **p<0.01; t-test.

Figure S4. *Lack of GlyRs mediated synaptic currents in PNs and GFP$^+$INs of layer V from P7 Glra2*KO *and WT mice.* **a**, representative traces showing GlyRs expression in PNs of the layer V at P7 in both WT and *Glra2*KO (scale bar 200 pA, 1 sec). **b**, representative traces showing the absence of GlyRs mediated currents in layer V PNs after bath application of excitatory and inhibitory blockers plus strychnine in WT and *Glra2*KO littermates at P7 (scale bar 5 pA, 1 s). Values are expressed as mean ± SEM, n=12 for WT and n=11 for *Glra2*KO neurons; t-test. **c**, representative traces showing GlyRs expression in GFP$^+$ INs of the layer V at P7 in both WT and *Glra2*KO (scale bar 200 pA, 1 sec). **d**, representative traces displaying the absence of GlyRs-mediated currents in layer V GFP$^+$ INs after bath application of excitatory and inhibitory blockers plus strychnine in WT and *Glra2*KO littermates at P7 (scale bar 5 pA, 1 s). Values are expressed as mean ± SEM, n=11 for WT and n=9 for *Glra2*KO interneurons; t-test.

Figure S5. *Developmental expression of GlyR subunits in WT and Glra2*KO *mice somatosensory cortex.* Relative expression of GlyR α and β subunits expressed in the somatosensory cortex during five distinct stages of cortical development. **a**, normalized developmental expression of all GlyRs

subunits in somatosensory cortices of WT mice. Values are normalized for the lowest expression of development (for α2 P30 while for the other subunits E16). **b**, developmental expression of α1 subunit in the somatosensory cortex in WT and *Glra2*KO. **c**, developmental expression of α2 subunit in the somatosensory cortex in WT mice. **d**, developmental expression of α3 subunit in the somatosensory cortex in WT and *Glra2*KO. **e**, developmental expression of α4 subunit in the somatosensory cortex in WT and *Glra2*KO. **f**, developmental expression of β subunit in the somatosensory cortex in WT and *Glra2*KO. Values are expressed as mean ± SEM, n=5 WT and 5 *Glra2*KO mice for E16, P0, P7, P30 n=4 WT and 4 *Glra2*KO mice for P14 using two-way Anova with Bonferroni post hoc test.

Supplemental experimental procedures

RNA preparation. RNA was isolated from mouse somatosensory cortex at different developmental stages and tissue was snap frozen. Total RNA extraction was performed by using RNeasy Plus mini kit (Qiagen, Germany) following manufacturer's instructions. Synthesis of cDNA was performed by High Capacity cDNA Reverse Transcription Kit (Applied Biosystem, Belgium) according to the protocol.

Quantitative real-time PCR (RT-PCR). cDNA amplification was performed using SYBR green master mix (Applied Biosystems) containing: 10mM forward and reverse primers, RNase free water and 12.5 ng cDNA template in a total reaction volume of 10 µl. Universal amplification conditions were used: initial denaturation for 20 seconds at 95 °C, followed by 40 cycles of 3 seconds at 95 °C and 30 seconds at 60 °C. Normalization of RT-PCR data was performed against the most stable reference genes as determined by GeNorm software for each age and developmental stage (Vandesompele et al., 2002). Hydroxymethylbilane synthase (HMBS), cyclophilin A (CYCA), hypoxanthine phosphoribosyl transferase (HPRT) and phosphoglycerate kinase 1 (PGK1) were used as reference genes for normalizing the expression of GlyRs during development. Relative quantification of gene expression was calculated using the comparative Ct method ($2^{-\Delta\Delta Ct}$). Specificity of PCR products was determined using melting curve analysis following the amplification protocol.

Oligonucleotides. The oligonucleotide primers used (Idt and Eurogentec, Belgium) were 5'-GATGGGCAACTGTACCTGACTG-3' and 5'-CTGGGCTCCTCTTGGAATG-3' for HMBS, 5'-GCGTCTCCTTCGAGCTGTT-3' and 5'-AAGTCACCACCCTGGCA-3' for CYCA, 5'-CTCATGGACTGATTATGGACAGGAC-3' and 5'-GCAGGTCAGCAAAGAACTTATAGCC-3' for HPRT, 5'-GAAGGGAAGGGAAAAGATGC-3' and 5'-GCTATGGGCTCGGTGTGC-3' for PGK1, 5'-GGAAGAGGCGACATCACAA-3' and 5'-TGGACATCCTCTCTCCGGAC-3' for α1 subunit, 5'-CACTGGCAAGTTTACCTGCAT-3' and 5'-GGAGACCCAGGACAAAATGA-3' for α2 subunit, 5'-GCACTGGAGAAGTTTTACCG-3' and 5'-AAGCAGGCTCGGGAGATGGTGTC -3' for α3 subunit, 5'-CAGCATCAGATTGACCCTCA-3' and 5'- GCAGGAGCATCTTCTAGCCA -3' for α4 subunit, 5'-CTGTTCATATCAGCACTTTGC-3' and 5'- GGGATGACAGGCTTGGCAG -3'

for the beta (Heck et al., 1997). The primers for α1, α2, α3, α4 were designed with Primer 3 software based on their annotations in National Center for Biotechnology information (http://www.ncbi.nlm.nih.gov/).

Immunohistochemistry. The number of GFP^+ cortical INs was evaluated in WT and *Glra2*KO P7 and P14 littermates born from breeding between Dlx 5-6 males and *Glra2*+/- females mice. Tbr1/Cux1 and Tbr1/Ctip2 labeling were performed as follow. Sections were washed three times for 5 min in PBS for rehydration of the samples. DNA denaturation and antigen retrieval was performed by incubation of the slides in citrate buffer for 20 min at 100°C. Following denaturation, slides were washed three times for 5 min in PBS. Blocking non-specific binding was performed by incubating slides 1 hour in PBS containing 10% normal donkey serum (NDS, Tremecula, USA) and 0.2% Triton X-100 (Sigma, Belgium). Primary goat anti-Cux1 (1:25; Sc-6327, Santa Cruz Biotechnologies, USA) or rat anti-Ctip2 (1:200; ab18465, Abcam, UK), and rabbit anti-Tbr1 (1:200; ab31940, Abcam, UK) were diluted in PBS and slices were incubated in the solution overnight. Secondary donkey anti-goat Alexa 488-555, donkey anti-rabbit Alexa 555-647 and donkey anti-rat Alexa 555-647 (A555, A647 and A488, Life Technologies, Belgium) dissolved in blocking solution were used at 1:500 for 1 hour at room temperature. Slides were mounted with DAPI-containing mounting medium (Vector Laboratories, USA) for counterstaining of nuclei. Similar protocol was applied for parvalbumin immunolabeling at P14: primary mouse anti-Parvalbumin (1:500, MAB 1572, Millipore, USA) was dissolved in 50% blocking solution and Alexa 555 was used as secondary antibody (A555 Life Technologies, Belgium). Calretinin and somatostatin were detected applying a similar (excepted antigen retrieval) protocol as well as GAD65 and PSD95 triple staining combined either with NeuN and Ctip2 or GFP using the following antibodies: mouse anti-calretinin (1:1000, mab1568, Millipore, USA) rat anti-somatostatin (1:50, mab354, Millipore, USA), mouse anti-GAD65 (5:100;Developmental studies hybridoma bank, USA) and rabbit anti-PSD95 (1:100; ab18258, Abcam, UK), mouse anti-NeuN clone A60 (1:100, Millipore, USA) and rabbit anti-NeuN (1:100, Millipore, USA) rabbit anti-GFP (1:200; ab6556, Abcam, UK). Double labeling were performed by one step co-incubation with a mixture of the appropriate antibodies. One step co-incubation was used for the secondary antibodies (Alexa, 1:500;

Life Technologies, Belgium). Triple labeling (NeuN/Ctip2 and either GAD65 or PSD95) were carried out with two-step incubation in which antibodies were firstly labelled for Ctip2/NeuN in which the antigen retrieval is required and then with the synaptic markers antibodies.

Herpes virus mediated gene transfer. Slice culture was carried out according previous literature adding some modifications (Cao et al., 2010). P7 littermates were sacrificed by decapitation and 300 µm slices were cut in filtered and oxygenated ACSF. Slice were then recovered at 34°C for 1 hour and placed in 6 well plates containing pre-warmed ACSF (34°C) and cell culture inserts (Millipore, Ireland). 0.6 µl of HSV specific for Dlx I expressing interneurons was pipetted twice directly over the somatosensory cortex and the slices were incubated for 1-3 days at 37° 5% CO_2. Afterwards, slices were moved to the recording chamber to test the specific interneuronal expression of the virus by patch clamp recordings. Slices were fixed overnight in 4% PFA and then stained with rabbit anti-PSD95 (1:100; ab18258, Abcam, UK).

Cortical thickness. P7 and P14 brain slices were used to measure cortical thickness in *Glra2*KO mice. Parallel lines from ventricles to the pial surface were used as reference to delineate a perpendicular line consisting in the thickness of dorsal (D), dorso-lateral (D-L) and lateral (L).

Golgi staining. P7 littermates were sacrificed by decapitation. Brains were dissected and washed several times in PBS. Staining was carried out using FD Rapid GolgiStain kit and protocol (FD Neurotechnologies Inc., Columbia USA). Images were obtained with a Nikon 80i Eclipse fluorescence microscope using oil immersion 100X objective. Fiji Image J was used for analysis.

Neuronal reconstruction. Biocytin-filled pipettes, during patch clamp experiments, were used to label either pyramidal neurons or GFP-expressing interneurons. 300 µm slices were removed from the recording chamber and fixed with 4% PFA for 1-2 hours. Afterwards, slices were rinsed 3 times with PBS and blocked using normal goat serum (NGS, Temecula, USA) 5% for 1 hour at RT. Streptavidin AlexaFluor 488 conjugate (S-11223, Life Technologies, Belgium) was used to label projection neurons whilst streptavidin AlexaFluor 555 conjugate (S-21381, Life Technologies, Belgium) for GFP-expressing interneurons. Biocytin-filled neurons and interneurons were reconstructed using

Neuromantic (freeware software by Myatt, D.R.) which was used to calculated branching points and total dendritic length. Sholl analysis was performed by using Fiji Image J plug-in and analyzed using the linear method (Schindelin et al., 2012, Ferreira et al., 2014). The distance from the soma to 300 μm was considered for the basal dendrites of PNs, while the distance from the apical dendrite to the end of the dendrites was used to measure the apical tufts of PNs. The distance from the soma to 300 μm was considered for GFP^- expressing interneurons. Spine and boutons density were calculated using Fiji ImageJ Simple Neurite Tracer and Cell Counter plug-in to measure respectively semi-automatically and manually the size and length of soma and dendrites and their number of spines and boutons (density= n/μm).

Confocal imaging. Images of labeled brain sections were acquired with a Carl Zeiss Axiovert 200M motorized microscope equipped with a LSM 510 META confocal laser scanner system (Carl Zeiss, Germany). For cell counting purposes, images were acquired with a Plan Apochromat Plan-Neofluar 40×/1.3 Oil DIC objectives. For neuronal reconstruction, Plan Apochromat 20×/0.75 was used to obtain z-stacks, while for spine density and PSD95 and GAD65 boutons the alpha plan-apochromat 100x/1.46. The A488 fluorophore was visualized by excitation with the 488 nm emission line of an Ar-Ion laser while the A555 and A647 dyes were visualized using the 543 nm spectral line of the He-Ne laser and the 633 nm spectral line of a second He-Ne laser, respectively. DAPI excitation was achieved by two-photon excitation at 750 nm with the light emitted by a mode locked MaiTai laser (Spectra Physics, USA). Z stacks were acquired every 1-1.5 μm. More than one Z-stack was acquire to capture the whole thickness of the cortex covering the same distance in the VZ. For neuronal reconstruction, Z-stacks were used to follow in depth and length the shape of the biocytin filled cells.

Cell counting and spine density. All cellular quantifications were performed in the brightest single plane along the Z-stack acquired with a 40× objective as described above. Analysis of cell counts in the developing somatosensory cortex at different ages was carried out using the manual cell counter tool included ImageJ. The dimension of analyzed field was either 450 × X μm or 225 × X μm according to the Y dimension changes between *Glra2*KO and WT and differences in age in order to

cover the entire cortex from the ventricle to the pial surface. Fiji Image J plugin was used for Sholl analysis and to count dendritic spines throughout the z-stack.

Statistics. All data are expressed as mean ± standard error of the mean (SEM). Mean and error calculations, as well as statistical analyses were computed in GraphPad (GraphPad Software, Inc). Unpaired t-test was used for most of the quantifications, while two-way Anova with Bonferroni post hocs was used for Sholl analysis, bin percentages of immunolabelings and developmental qPCR for GlyRs.

Cao JL, Vialou VF, Lobo MK, Robison AJ, Neve RL, Cooper DC, Nestler EJ, Han MH. 2010. Essential role of the cAMP-cAMP response-element binding protein pathway in opiate-induced homeostatic adaptations of locus coeruleus neurons. Proceedings of the National Academy of Sciences of the United States of America 107:17011-17016.

Ferreira TA, Blackman AV, Oyrer J, Jayabal S, Chung AJ, Watt AJ, Sjostrom PJ, van Meyel DJ. 2014. Neuronal morphometry directly from bitmap images. Nature methods 11:982-984.

Schindelin J, Arganda-Carreras I, Frise E, Kaynig V, Longair M, Pietzsch T, Preibisch S, Rueden C, Saalfeld S, Schmid B, Tinevez JY, White DJ, Hartenstein V, Eliceiri K, Tomancak P, Cardona A. 2012. Fiji: an open-source platform for biological-image analysis. Nature methods 9:676-682.

Figure S1

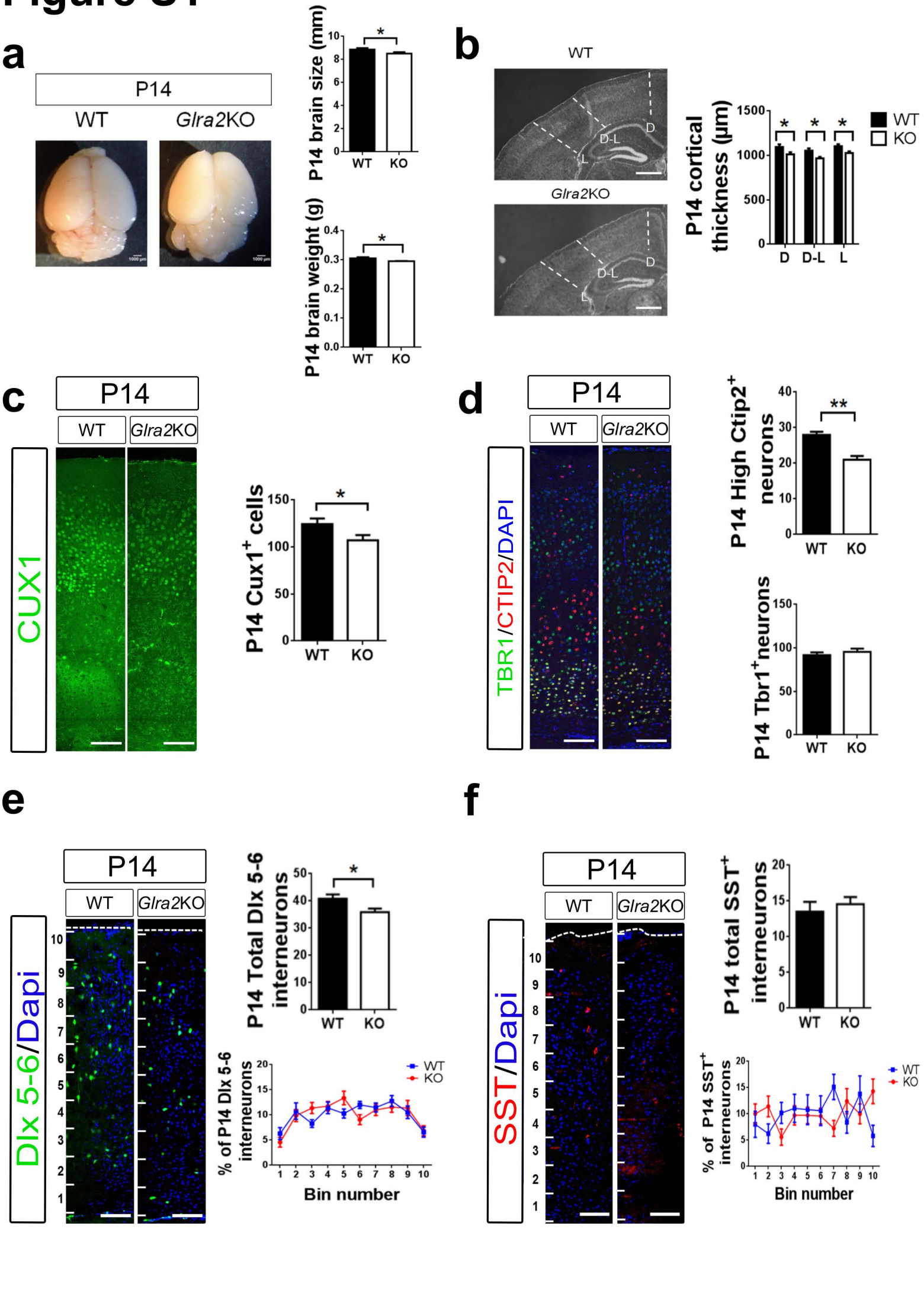
a
P14
WT
Glra2KO
P14 brain size (mm)
P14 brain weight (g)
WT
KO
b
WT
Glra2KO
D
D-L
L
P14 cortical thickness (µm)
c
P14
CUX1
P14 Cux1+ cells
d
TBR1/CTIP2/DAPI
P14 High Ctip2+ neurons
P14 Tbr1+neurons
e
Dlx 5-6/Dapi
P14 Total Dlx 5-6 interneurons
% of P14 Dlx 5-6 interneurons
Bin number
f
SST/Dapi
P14 total SST+ interneurons
% of P14 SST+ interneurons

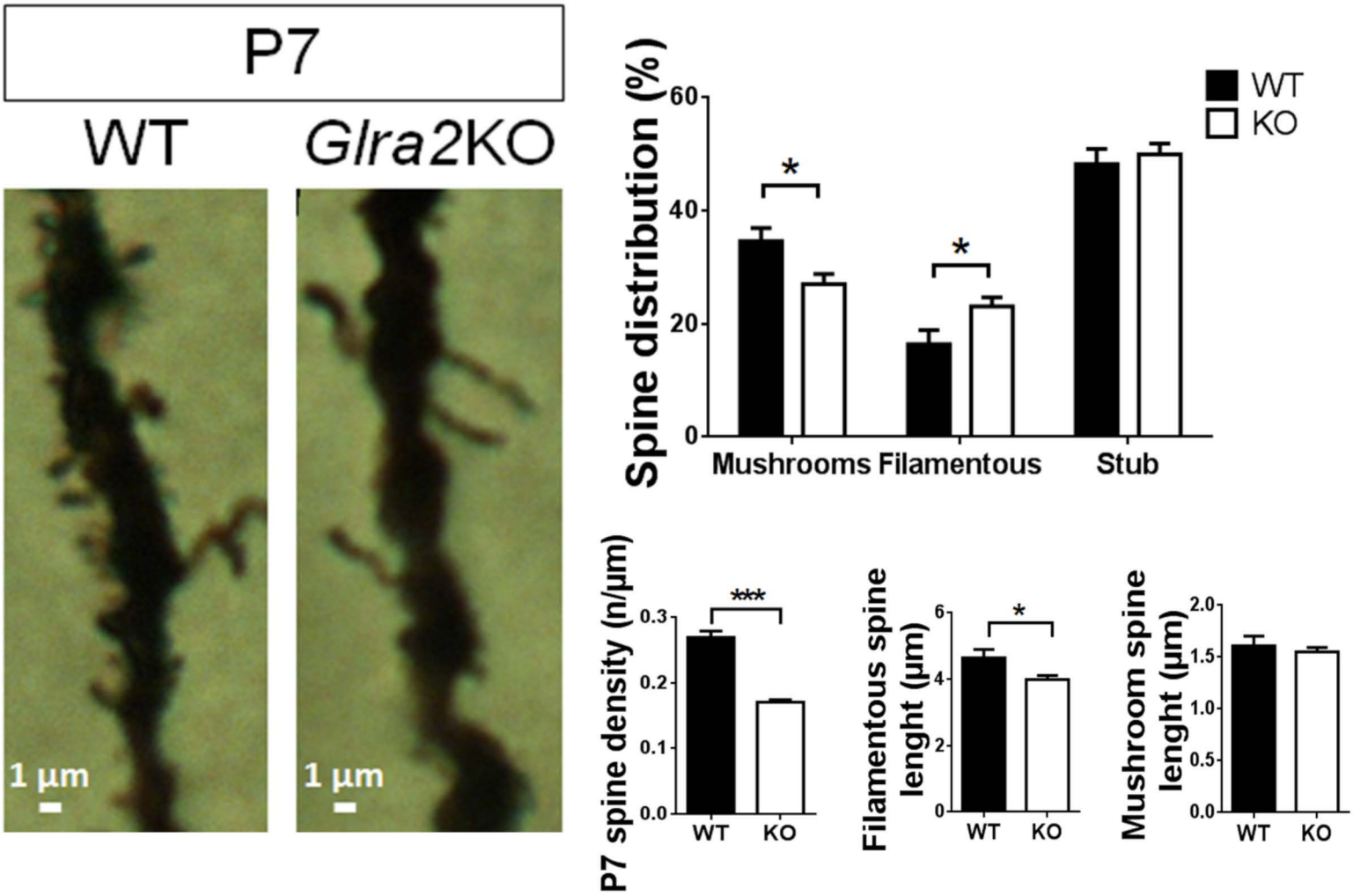
P7
WT
Glra2KO
1 µm
1 µm
Spine distribution (%)
60
40
20
0
WT
KO
*
*
Mushrooms
Filamentous
Stub
P7 spine density (n/µm)
0.3
0.2
0.1
0.0
***
WT
KO
Filamentous spine lenght (µm)
6
4
2
0
*
WT
KO
Mushroom spine lenght (µm)
2.0
1.5
1.0
0.5
0.0
WT
KO

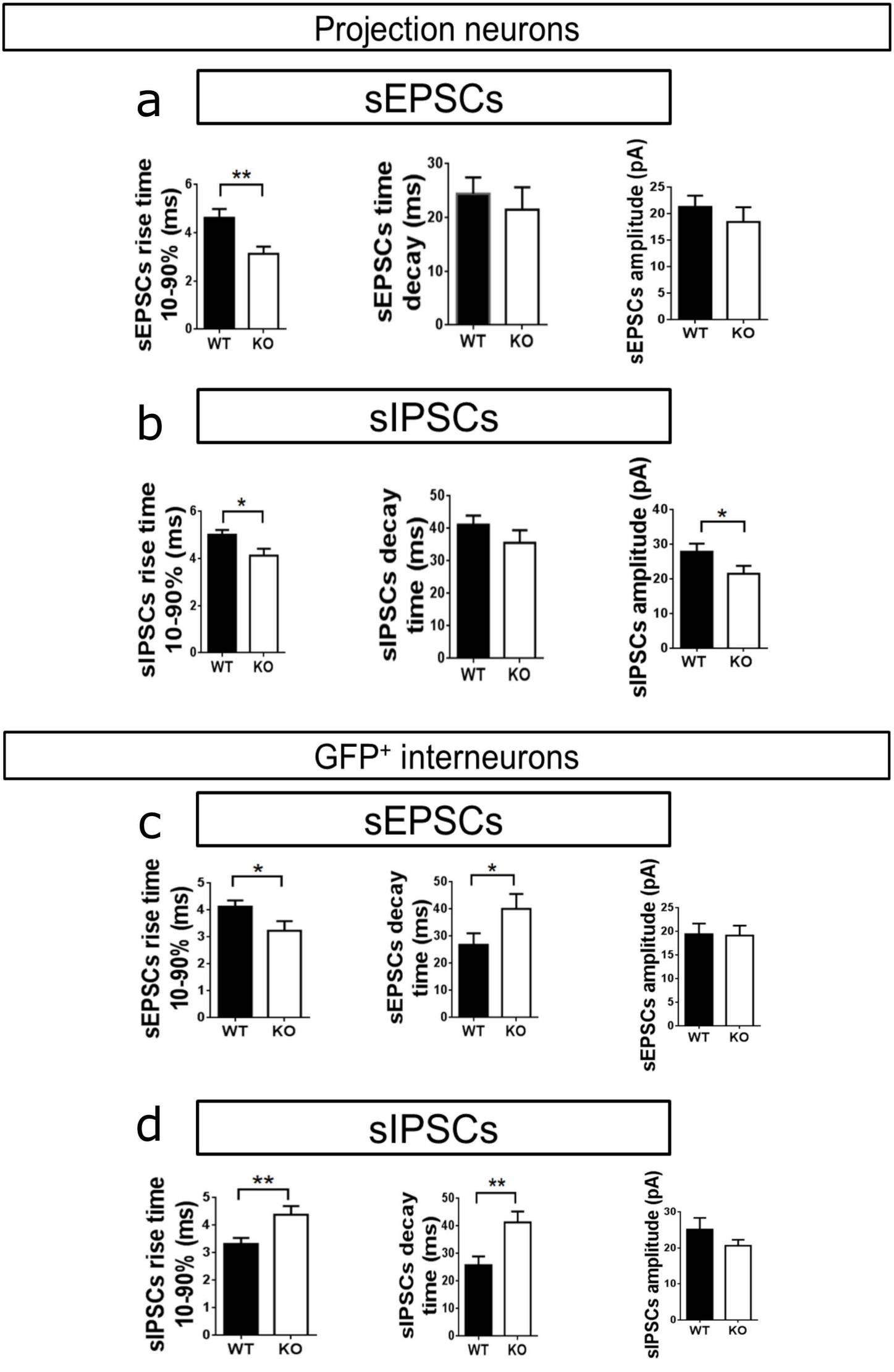
Projection neurons
a
sEPSCs
sEPSCs rise time 10-90% (ms)
**
WT
KO
sEPSCs time decay (ms)
sEPSCs amplitude (pA)
b
sIPSCs
sIPSCs rise time 10-90% (ms)
*
sIPSCs decay time (ms)
sIPSCs amplitude (pA)
GFP+ interneurons
c
sEPSCs
d
sIPSCs

Projection neurons

a

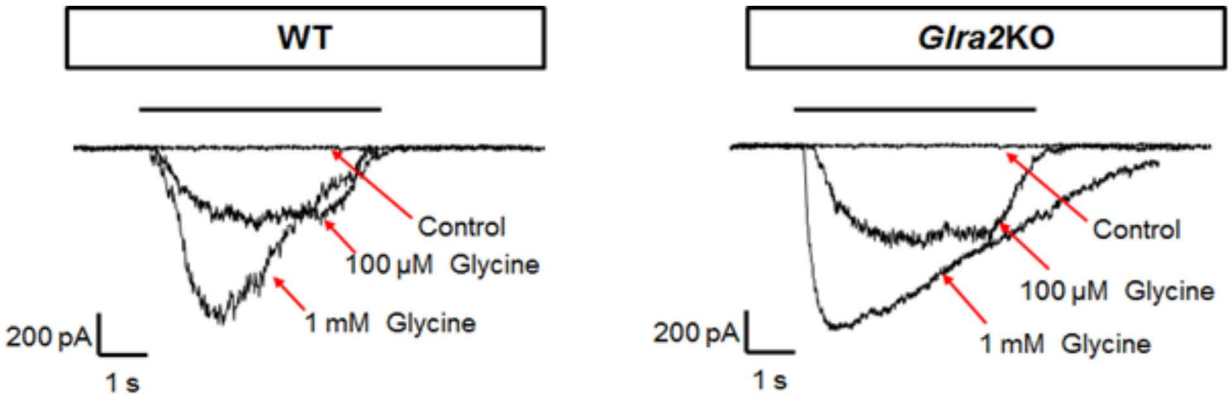

b

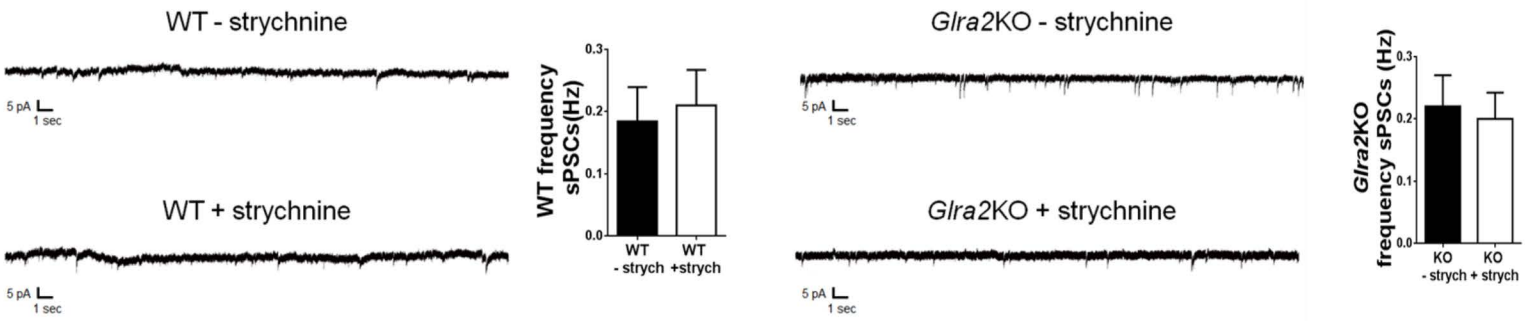

GFP+ interneurons

c

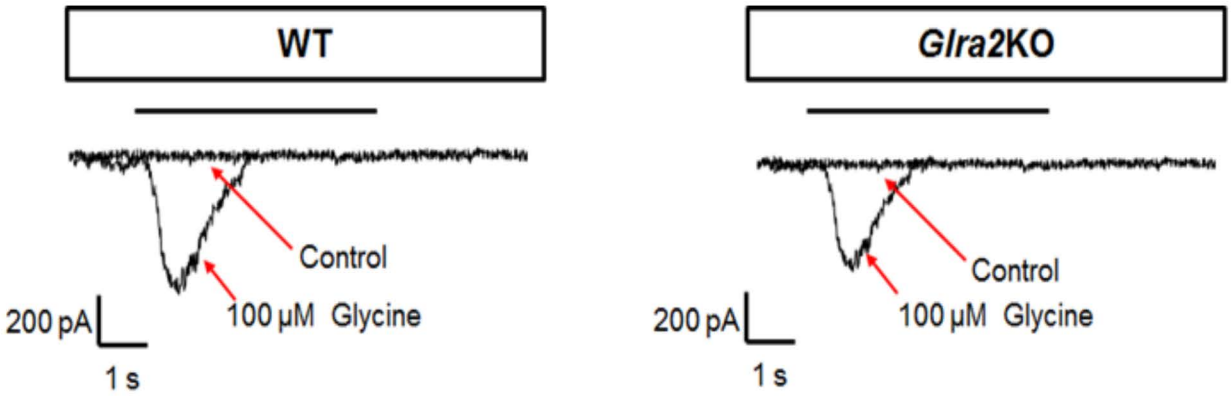

d

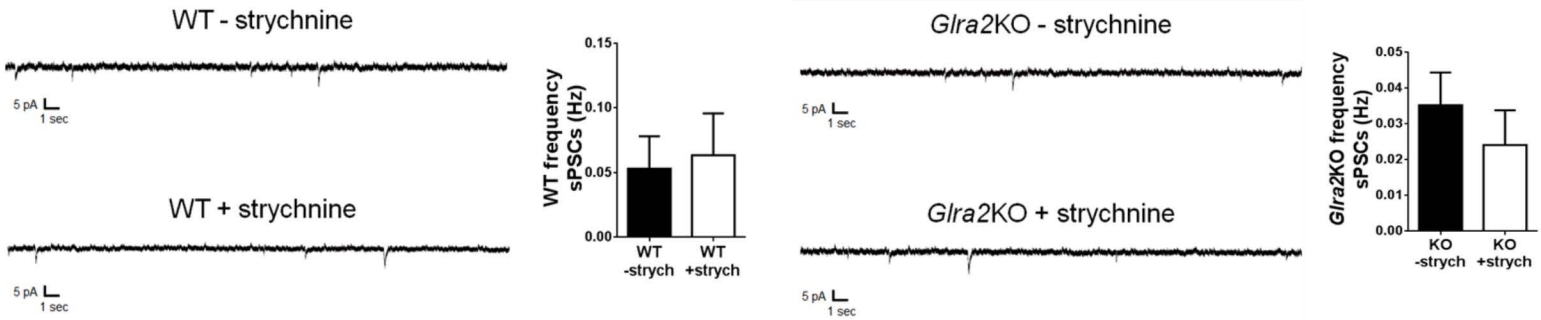

a

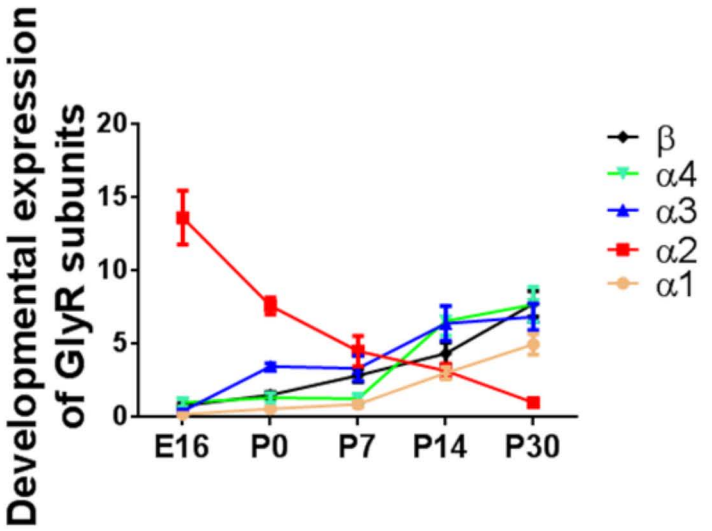
Developmental expression of GlyR subunits
20
15
10
5
0
E16
P0
P7
P14
P30
β
α4
α3
α2
α1

b

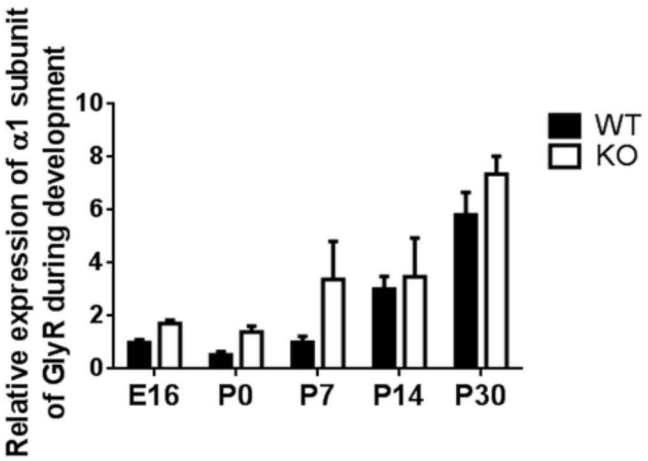
Relative expression of α1 subunit of GlyR during development
10
8
6
4
2
0
E16
P0
P7
P14
P30
WT
KO

c

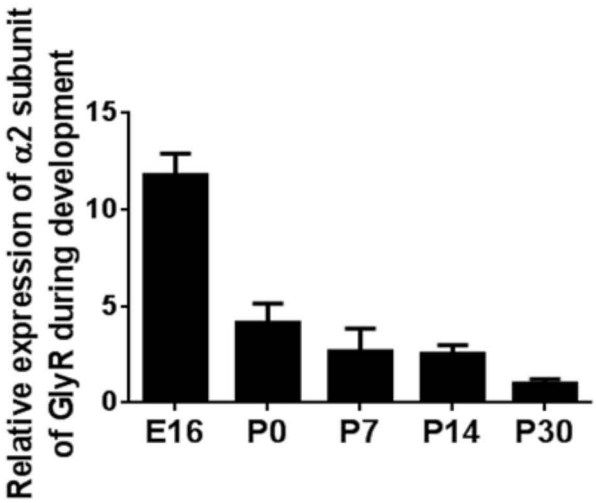
Relative expression of α2 subunit of GlyR during development
15
10
5
0
E16
P0
P7
P14
P30

d

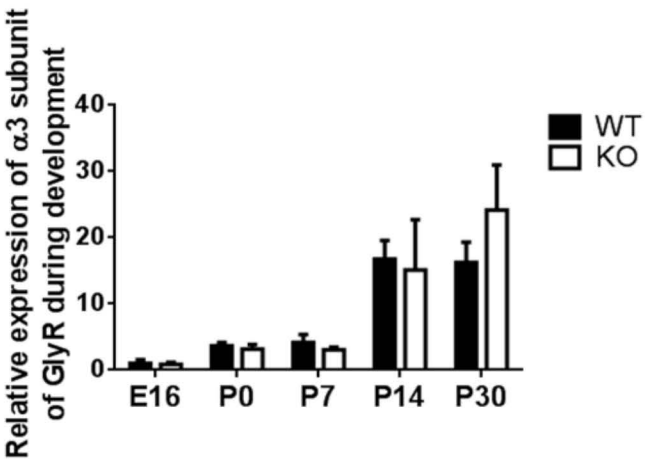
Relative expression of α3 subunit of GlyR during development
40
30
20
10
0
E16
P0
P7
P14
P30
WT
KO

e

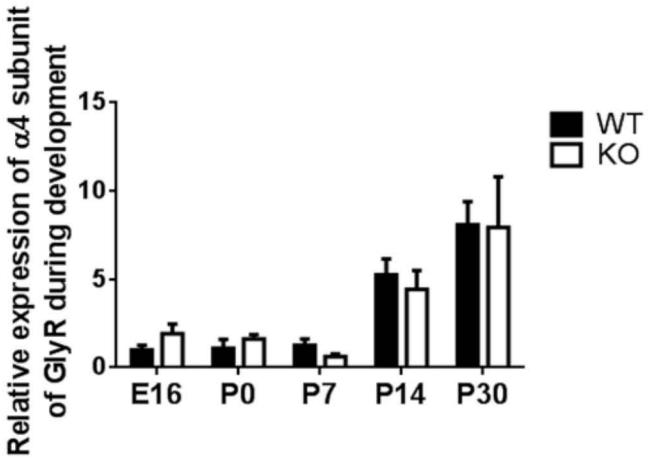
Relative expression of α4 subunit of GlyR during development
15
10
5
0
E16
P0
P7
P14
P30
WT
KO

f

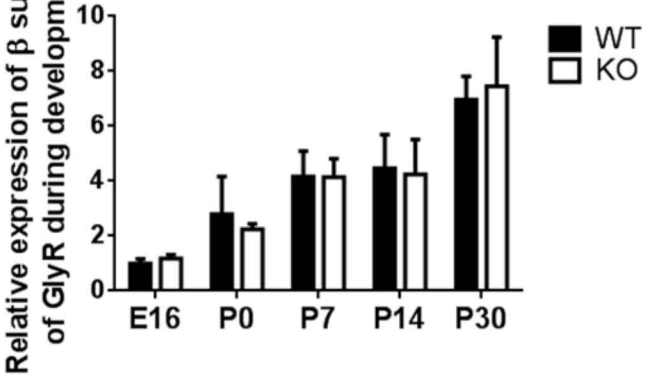
Relative expression of β subunit of GlyR during development
10
8
6
4
2
0
E16
P0
P7
P14
P30
WT
KO